Chromatin accessibility maps of chronic lymphocytic leukemia identify subtype-specific epigenome signatures and transcription regulatory networks

André F. Rendeiro[1,*], Christian Schmidl[1,*], Jonathan Strefford[2,*], Renata Walewska[3], Zadie Davis[3], Matthias Farlik[1], David Oscier[3], Christoph Bock[1,4,5,♯],

[1]CeMM Research Center for Molecular Medicine of the Austrian Academy of Sciences, Vienna, Austria

[2]Cancer Genomics, Cancer Sciences, University of Southampton, Southampton, UK

[3]Department of Molecular Pathology, Royal Bournemouth Hospital, Bournemouth, UK

[4]Department of Laboratory Medicine, Medical University of Vienna, Vienna, Austria

[5]Max Planck Institute for Informatics, Saarbrücken, Germany

[*]These authors contributed equally to this work

Abstract

Chronic lymphocytic leukemia (CLL) is characterized by substantial clinical heterogeneity, despite relatively few genetic alterations. To provide a basis for studying epigenome deregulation in CLL, we established genome-wide chromatin accessibility maps for 88 CLL samples from 55 patients using the ATAC-seq assay, and we also performed ChIPmentation and RNA-seq profiling for ten representative samples. Based on the resulting dataset, we devised and applied a bioinformatic method that links chromatin profiles to clinical annotations. Our analysis identified sample-specific variation on top of a shared core of CLL regulatory regions. IGHV mutation status – which distinguishes the two major subtypes of CLL – was accurately predicted by the chromatin profiles, and gene regulatory networks inferred for IGHV-mutated vs. IGHV-unmutated samples identified characteristic differences between these two disease subtypes. In summary, we discovered widespread heterogeneity in the chromatin landscape of CLL, established a community resource for studying epigenome deregulation in leukemia, and demonstrated the feasibility of chromatin accessibility mapping in cancer cohorts and clinical research.

Introduction

Chronic lymphocytic leukemia (CLL) is the most common type of leukemia in the Western world[1]. It is characterized by remarkable clinical heterogeneity, with some patients pursuing an indolent course while others progress rapidly and require early treatment. The diverse clinical course of CLL patients, particularly those that initially present with low disease burden, fuels interest in prognostic biomarkers and personalized therapies[2]. Current clinical biomarkers for CLL include mutational status of the IGHV genes[3,4], IGHV gene family usage[5], stereotyped B cell receptors[6,7], serum markers[8,9], chromosomal aberrations[10,11], and somatic mutations[12,13,14]. Most notably, IGHV mutation status distinguishes between a less aggressive form of CLL with mutated IGHV genes (mCLL) and a more aggressive form

with unmutated IGHV genes (uCLL). Several surrogate biomarkers of IGHV mutation status have been described. For example, high levels of ZAP70 expression appear to be associated with uCLL [15]. In addition to these focused biomarkers, transcriptome profiling has been used to define broader molecular signatures that may improve disease stratification independent of IGHV mutation status [16].

Recent genome and exome sequencing projects have identified additional genes that are recurrently mutated in CLL [17,18], some of which have prognostic significance. Nevertheless, CLL samples carry relatively few genetic aberrations compared to other adult cancers [19], and some patients develop progressive disease despite being classified as "low risk" based on genetic markers, suggesting that non-genetic factors are relevant for CLL etiology and outcome. Several lines of evidence point to a role of epigenome deregulation in CLL pathogenesis: First, somatic mutations have been observed in non-coding regions of the genome, where they appear to induce deregulation of relevant cancer genes [18]. Second, chromatin remodeling proteins such as ARID1A and CHD2 are recurrently mutated in CLL [17,18], indicating causal links between chromatin deregulation and CLL. Third, aberrant DNA methylation was observed in all studied CLL patients [20,21,22], correlated with IGHV mutation status, and identified a new subtype (iCLL) that appears to be an intermediate between mCLL and uCLL [20,23].

While prior studies of epigenome deregulation in primary cancer samples have focused almost exclusively on DNA methylation [24], recent technological advances now make it possible to map chromatin landscapes in large patient cohorts. Most notably, the assay for transposase-accessible chromatin using sequencing (ATAC-seq) facilitates open chromatin mapping in scarce clinical samples [25], and ChIPmentation provides a streamlined, low-input workflow for genome-wide mapping of histone marks and transcription factors [26]. These two assays use a hyperactive variant of the prokaryotic Tn5 transposase, which integrates DNA sequencing adapters preferentially in genomic regions with accessible chromatin. ATAC-seq profiles are similar to those of DNase-seq, sharing the ability to detect footprints of transcription factor binding in the chromatin accessibility landscape [27]. ChIPmentation closely recapitulates the results obtained by more classical chromatin immunoprecipitation followed by sequencing (ChIP-seq) protocols [26]. Both assays work well on scarce patient samples, and they enable fast sample processing on timescales that would be compatible with routine clinical diagnostics.

To establish the feasibility of large-scale chromatin analysis in primary cancer samples, and to provide a basis for dissecting regulatory heterogeneity in CLL, we performed chromatin accessibility mapping using the ATAC-seq assay on a cohort of 88 primary CLL samples derived from 55 patients. Furthermore, for ten of these samples we established histone profiles using ChIPmentation for three histone marks (H3K4me1, H3K27ac, H3K27me3) and transcriptome profiles using RNA-seq. We also developed a bioinformatic method for linking these chromatin profiles to clinical annotations and molecular diagnostics data, and we performed an initial analysis of gene regulatory networks that underlie the major disease subtypes of CLL. In summary, this study provides a publicly available reference dataset and a rich source of testable hypotheses for dissecting CLL biology and pathogenesis.

Results

Chromatin accessibility maps for 88 CLL samples

To map the chromatin accessibility landscape of CLL (Figure 1a), we performed ATAC-seq on 88 purified lymphocyte samples obtained from the peripheral blood of 55 CLL patients. These patients were managed at a single medical center, and they collectively represent the spectrum of clinical phenotypes that are commonly observed in CLL (Supplementary Data 1). Their average age at sample collection was 73 years, and 8% of patients were under treatment when the samples were collected. The majority of samples (58%)

had been classified as IGHV-mutated as part of routine clinical diagnostics (Supplementary Figure 1 and Supplementary Data 1).

All samples selected for ATAC-seq library preparation contained at least 80% leukemic cells. The ATAC-seq libraries were sequenced with an average of 25.4 million fragments, resulting in a dataset comprising a total of 2.2 billion sequenced fragments (Supplementary Data 2). Data quality was high in all cases, with mitochondrial read rates in the expected range for ATAC-seq (mean: 38.3%; standard deviation: 9.3) and the characteristic patterns of nucleosome phasing derived from paired-end data (Supplementary Figure 2). The individual samples were sequenced with sufficient depth to recover the majority of chromatin-accessible regions that are detectable in each sample (Supplementary Figure 3). Moreover, by combining data across all 88 samples we approached cohort-level saturation in terms of unique chromatin-accessible regions (Figure 1b), indicating that our cohort is sufficiently large to identify most regulatory regions that are common in CLL samples.

As illustrated for the BLK gene locus (Figure 1c), our ATAC-seq dataset can be aggregated into a comprehensive map of chromatin accessibility in CLL. This map comprises 112,298 candidate regulatory regions, of which 11.6% are constitutively open across essentially all CLL samples, whereas 59.1% are open in a sizable proportion of samples (5% to 95% of samples), and 29.3% are unique to only one or very few samples (Supplementary Figure 4a). All data are available for interactive browsing and download from the supplementary website (http://cll-chromatin.computational-epigenetics.org/).

Chromatin-accessible regions in CLL are widely distributed throughout the genome, with moderate enrichment at genes and promoters (Figure 1d and Supplementary Figure 4b). We also compared the CLL-accessible regions to epigenome segmentations for CD19+ B cells (Figure 1e and Supplementary Figure 4c), a related cell type for which comprehensive reference epigenome data are publicly available [28]. Strong enrichment was observed for regions that are classified as transcription start sites or as enhancer elements in the B cells, indicative of a globally similar chromatin accessibility landscape between B cells and CLL. Nevertheless, a sizable fraction of CLL-accessible regions carried quiescent or repressive chromatin in B cells, which is the expected pattern for regulatory elements that are subject to CLL-specific activation.

Heterogeneity in the CLL chromatin accessibility landscape

Although the number of constitutively accessible regions in our cohort was relatively low (11.6%, Supplementary Figure 4a), we still observed high consistency between individual samples, and any two samples in our dataset shared 70% to 98% of their chromatin-accessible regions (Supplementary Figure 5a). Conversely, we also observed robust differences in the ATAC-seq signal intensity between samples. To facilitate gene-by-gene investigation of this heterogeneity, we established the "chromatin accessibility corridor" as a means of aggregating the cohort-level variation into a single intuitive genome browser track (Figure 2a and Supplementary Website). As illustrated by the PAX5 and BCL6 gene loci, even where the locations of chromatin accessible regions are shared across most samples, substantial differences in the ATAC-seq intensity levels were observed (Figure 2a).

For a more systematic investigation of chromatin heterogeneity in CLL, we calculated the cohort-level variance for each of the 112,298 regions in the CLL consensus map and linked these regions to nearby genes that they may regulate (see Methods for details). Promoters of genes with a known role in B cell biology and/or CLL pathogenesis showed significantly reduced variability ($p < 10\text{-}5$, Kolmogorov-Smirnov test; Supplementary Figure 5b), which was not due to differential representation of CpG islands among the promoters of the gene sets ($p = 0.49$, Fisher's exact test). For distal enhancer elements we did not observe any clear differences in heterogeneity between genes with and without a link to B cells and CLL ($p = 0.08$, Kolmogorov-Smirnov test).

Beyond these global trends, the variance and distribution of chromatin accessibility across samples was highly gene-specific (Figure 2b and Supplementary Figure 5c), as illustrated by CLL-linked genes including B cell surface markers (CD19), B cell receptor signaling components (CD79A/B, LYN, BTK), common oncogenes (MYCN, KRAS, NRAS), and genes that are recurrently mutated in CLL (NOTCH1, SF3BP1, XPO1, CDKN1B)[29,18,17]. Unsupervised principal component analysis clearly identified IGHV mutation status as the major source of heterogeneity in chromatin accessibility among CLL samples (Figure 2c and Supplementary Figure 6). However, the first two principal components explained only 6.8% and 5.2% of the total variance in the chromatin accessibility dataset, suggesting that many other factors contribute to the observed differences between samples.

The most direct way by which differences in chromatin accessibility may influence disease course would be through differential regulation of CLL-relevant genes. Therefore, to systematically assess the link between chromatin accessibility and gene expression in our cohort, we performed RNA-seq on ten of the CLL samples with matched ATAC-seq data. A weak positive correlation was observed between chromatin accessibility and gene expression (Pearson's r = 0.3; Supplementary Figure 7a), which was highly dependent on the distance of the chromatin-accessible region to the nearest transcription start site (Supplementary Figure 7b).

For chromatin-accessible regions in the vicinity of genes that RNA-seq identified as differentially expressed between IGHV-mutated (mCLL) and IGHV-unmutated (uCLL) samples (Supplementary Data 3), we observed significant differences in chromatin accessibility, which provided partial separation of the two disease subtypes (Supplementary Figure 7c). A more pronounced separation was observed when we focused our analysis on those regions that had been identified as differentially methylated between mCLL and uCLL in a prior study of DNA methylation in CLL[20] (Supplementary Figure 7d).

Finally, we assessed whether patterns of differential variability between mCLL and uCLL (i.e., higher levels of heterogeneity in one or the other subtype) may provide insights into the biology of these two disease subtypes. We identified 389 regions that showed a higher degree of variability among mCLL samples, whereas 581 regions were more variable among uCLL samples (Supplementary Figure 8a) – consistent with prior results showing higher gene expression variability among uCLL samples[30]. These differentially variable regions were distributed across a broad range of ATAC-seq intensity values, and they were not a side effect of differences in average chromatin accessibility (Supplementary Figure 8b). Genomic region enrichment analysis using the LOLA software[31] found mCLL-variable regions enriched for B cell specific transcription factor binding (ATF2, BATF, BCL6, NFKB, RUNX3) and active histone marks (Supplementary Figure 8c). In contrast, uCLL-variable regions were strongly associated with the cohesin complex, including binding sites for CTCF, RAD21, and SMC3.

Disease subtype-specific patterns of chromatin accessibility

To link the CLL chromatin accessibility landscape to clinical annotations and molecular diagnostics data (most notably to the IGHV mutation status that distinguishes between mCLL and uCLL), we devised a machine learning based method that derives subtype-specific signatures directly from the data (Figure 3a). Random forest classifiers were trained to predict whether a sample is IGHV-mutated or IGHV-unmutated, based on the chromatin accessibility values for all 112,298 regions in the CLL consensus map. We evaluated the performance of the resulting classifier by leave-one-out cross-validation and observed excellent prediction accuracy with a ROC area under curve of 0.96 (Figure 3b), which corresponds to a sensitivity of 95.6% at a specificity of 88.2%. To confirm that this cross-validated test set performance was not inflated by any form of overtraining, we repeated the same predictions one thousand times with randomly shuffled class labels. Much lower ROC area under curve values were observed in all cases, and their mean was very close to the theoretical expectation of 0.5 (Figure 3b).

Next, we extracted the most predictive regions from the trained classifiers, giving rise to data-driven chromatin signatures that discriminate between mCLL and uCLL (Supplementary Data 4). Hierarchical clustering categorized these regions into 719 with increased chromatin accessibility in IGHV-mutated samples ("mCLL regions", cluster 1 in Figure 3c) and 764 regions with increased chromatin accessibility in IGHV-unmutated samples ("uCLL regions", cluster 2 in Figure 3c). 51% of these machine learning based signature regions overlapped with statistically significant differential ATAC-seq peaks between IGHV-mutated and IGHV-unmutated samples (Supplementary Figure 9a and Supplementary Data 4, see Methods for details). The remaining regions contributed to accurate prediction of CLL subtypes as part of a broader signature even though they did not by themselves reach the stringent thresholds of the differential peak analysis (Supplementary Figure 9b).

To test whether these subtype-specific chromatin signatures reflected more general differences in the gene regulatory landscape of CLL, we compared RNA-seq profiles as well as ChIPmentation maps for three histone marks (H3K4me1, H3K27ac, H3K27me3) between five IGHV-mutated and five IGHV-unmutated samples. We found that the genes in the vicinity of the signature regions were on average more highly expressed in the cell type showing higher chromatin accessibility (Figure 3d and Supplementary Figure 10), although only a small percentage of these genes were significantly differentially expressed between mCLL and uCLL samples based on our RNA-seq data (0.8% and 6.3% respectively). Moreover, the ChIPmentation profiles were consistently associated with the differences in chromatin accessibility. Higher levels of the active H3K27ac mark as compared to repressive H3K27me3 were found in mCLL samples and mCLL-specific regions, and vice versa for uCLL (Figure 3e). This observation is illustrated by the ZNF667 promoter and an enhancer at the ZBTB20 locus (Figure 3f), two genes that have been identified as predictors of time to treatment and overall survival in CLL [32,33]. Between individual samples we observed both qualitative (i.e., presence or absence of a peak) and quantitative (i.e., different peak height) differences in chromatin accessibility, and some of the most consistent differences between mCLL and uCLL affected genes with a known role in CLL (Supplementary Figure 11 and 12). For example, the expression ratio between ADAM29 and LPL has been shown to have prognostic value in CLL [34], and our dataset identifies an mCLL-specific chromatin-accessible region within the ADAM29 locus (Supplementary Figure 11) as well as a uCLL-specific chromatin-accessible region overlapping with the LPL promoter (Supplementary Figure 12), which may provide a regulatory basis for the previously described association. CD83, which has been associated with treatment-free survival [35], is another example of a gene locus containing an mCLL-specific chromatin-accessible region (Supplementary Figure 11). In contrast, uCLL-specific regions were identified in the gene loci encoding the CLL-linked transcription factor CREBBP [18] and the surface protein CD38, which has been extensively validated as a prognostic factor in CLL [36] (Supplementary Figure 12).

To gain insight into the more general biological characteristics of the mCLL and uCLL signature regions, we performed genomic region set analysis using LOLA [31] (Figure 3g), and we observed that the mCLL regions were enriched for active promoter and enhancer regions (marked by H3K4me1 and H3K27ac) in lymphocyte-derived cell lines (SU-DHL-5, JVM-2, GM12878, and KARPAS-422) as well as binding sites of relevant transcription factors (BATF, BCL6, and BLC3). In contrast, the uCLL regions were enriched for H3K4me1-marked promoter/enhancer regions in CD38-negative naïve B cells, reflecting the postulated naïve B cell origin of these CLL cells [37]. The uCLL regions were also enriched for transcribed regions (H3K36me3) in naïve B cells and in B cell-derived cell lines such as the BL-2 cell line, which has not undergone class-switch recombination.

We also performed motif enrichment analysis for the mCLL and uCLL signature region sets and observed significant enrichment relative to a random background model but no clear-cut differences when comparing the two region sets directly with each other (which is expected given the low statistical power of such an analysis). Nevertheless, when we linked chromatin-accessible regions to co-localized genes, we observed strong differences in the enrichment for cellular signaling pathways (Figure 3h). The mCLL regions were

associated with pathways having an established role in normal lymphocytes (CTLA4 inhibitory signaling, high-affinity IgE receptor signaling, Fc epsilon signaling, and Fc gamma receptor signaling), while the uCLL regions were associated with cancer-associated pathways such as NOTCH signaling and FGF receptor signaling. All of these enrichment analyses were validated based on the statistically significant differential ATAC-seq peaks between IGHV-mutated and IGHV-unmutated samples, which gave rise to highly similar results (Supplementary Figure 13).

Finally, we investigated whether a third CLL subtype – termed IGHV intermediate (iCLL) – could be detected in our dataset, as it was recently proposed based on DNA methylation data [20,23]. Clustering all samples based on the IGHV mutation signature regions, we indeed observed two intermediate clusters, the larger one comprising 20 samples from 14 patients (Figure 4a, green) and the smaller one comprising 3 samples from 2 patients (Figure 4a, brown). Most but not all of these iCLL samples were classified as IGHV-mutated based on the available molecular diagnostics data (Supplementary Figure 14). Principal component analysis provided further evidence that the iCLL samples fall between mCLL and uCLL samples based on their ATAC-seq profiles (Figure 4b). Their intermediate character was also supported by the RNA-seq and ChIPmentation data, where the iCLL group showed patterns that consistently ranged between those of the mCLL and uCLL groups (Supplementary Figure 15).

Gene regulatory networks underlying the mCLL and uCLL disease subtypes

In addition to providing chromatin accessibility maps, ATAC-seq can also detect transcription factor binding based on characteristic chromatin footprints [25]. Using this property of our data, we inferred chromatin-based gene regulatory networks for CLL and its two major disease subtypes (Figure 5a). To that end, we pooled all ATAC-seq data across the analyzed samples, identified footprints for 366 transcription factors with high-quality motifs in the JASPAR database [38], and linked these regulatory elements to their putative target genes (see Methods for details). The quality of the observed footprints was comparable to those in publicly available DNase-seq data for CD19+ B cells (Supplementary Figure 16), although we observed some deviations between the two assays that are likely due to the different sequence specificity of the Tn5 enzyme as opposed to the DNase I enzyme.

We first inferred a pan-CLL gene regulatory network using ATAC-seq data from all samples (Supplementary Figure 17). The resulting network was dominated by highly connected transcription factors, including broadly activating factors (SP1/2/3), the insulator protein CTCF, and regulators of biological processes such as cell proliferation (EGR), cell cycle (E2F), and B cell maturation (SPI1, PAX5). This pan-CLL network was structurally similar to a network for CD19+ B cells that we inferred from publicly available DNase-seq data using the same bioinformatic method (Supplementary Figure 18), and in the absence of a large chromatin accessibility dataset of B cells from healthy individuals it is not possible to conclusively identify the CLL-specific parts of our network.

Second, in order to investigate regulatory differences between CLL subtypes, we inferred gene regulatory networks separately for mCLL and uCLL samples (Supplementary Figure 19) and identified the most differentially connected genes between the two (Figure 5b). Genes that were more highly connected in the mCLL network coded for the transcription factors ZNF354C and ELF5, the metallopeptidase ADAM29, and the membrane protein CD22. In contrast, the BMP receptor CRIM1, the transcription factors MECOM and PAX9, the FGF signaling receptor FGFR1, and the membrane protein CD9 were more highly connected in the uCLL network (Figure 5c). The more highly connected genes in either subtype also showed higher levels of H3K4me1 and H3K27ac in their regulatory elements in samples of the corresponding subtype (Supplementary Figure 20a and 20b).

When we restricted our analysis to genes with a known role in B cell biology and/or CLL pathogenesis (Figure 5d), we observed a highly specific association of CD22 (which codes for an inhibitory receptor

involved in B cell receptor signaling) with mCLL, whereas CD38 and ZAP70 were preferentially associated with uCLL. Focusing on CD22 and PAX9 as two high-ranking genes in our analysis, we plotted the sub-networks of their direct neighbors and observed characteristic differences between the gene regulatory networks for mCLL and uCLL (Supplementary Figure 20c). Many of the subtype-specific genes identified by the regulatory network also showed locus-specific differences in their ChIPmentation profiles (Supplementary Figure 20d). Altogether, our results confirm that ATAC-seq profiles are useful for identifying epigenome differences in clinical samples, and they illustrate how this dataset can be used for deriving testable hypotheses about the regulatory basis of CLL.

Discussion

By ATAC-seq profiling on a large set of primary CLL samples, we have established a detailed map of the chromatin accessibility landscape in CLL. The ATAC-seq data were complemented by RNA-seq profiles and ChIPmentation for three histone marks, performed in ten representative samples covering three disease subtypes (mCLL, uCLL, iCLL). To our knowledge, this dataset is currently the largest catalog of chromatin accessibility maps for any cancer type, demonstrating the feasibility of chromatin profiling in large cohorts of primary cancer samples and validating a broadly applicable bioinformatics workflow for analyzing such data.

The large number of patient samples included in this study allowed us to dissect the role of epigenome variability as a potential contributor to cancer heterogeneity [39]. We found that variability between samples was common in our dataset, both in the form of qualitative (i.e., presence or absence of a peak) and quantitative (i.e., different peak height) differences between individual samples. In the absence of a reference dataset with chromatin accessibility maps for normal B cells from a large number of healthy donors, it remains unclear whether or not the observed heterogeneity in CLL constitutes a major increase over the expected heterogeneity in a genetically diverse cohort. Nevertheless, significantly reduced heterogeneity at the promoters of genes involved in B cell biology and/or CLL pathogenesis suggest a functional role of the observed inter-individual differences. Overall, our data support the existence of a core regulatory landscape shared by most or all CLL samples, which is complemented by sample-specific subsets of a substantially larger number of CLL-associated regulatory regions.

IGHV mutation status was the single biggest contributor to sample-specific differences in chromatin accessibility, although it explained only 5-10% of the observed variance in our dataset. Based on the ATAC-seq profiles we were able to distinguish with excellent accuracy between IGHV-mutated mCLL and IGHV-unmutated uCLL. Our analysis also suggested the existence of one (or possibly two) intermediate types (iCLL), consistent with a recent report that used DNA methylation analysis of a large CLL cohort to identify novel CLL subtypes [20]. Chromatin accessibility and DNA methylation both appear to separate better between these disease subtypes than gene expression data, suggesting that the biological differences between the major subtypes of CLL are primarily encoded in the epigenome and possibly reflect patterns retained from a subtype-specific cell-of-origin.

Combining data across samples provided sufficient sequencing depth for footprinting analysis of transcription factor binding, allowing us to infer gene regulatory networks from the data and to compare them between mCLL and uCLL. Although genomic footprinting has its limitations [40], the resulting network models give rise to predictions that can provide a starting point for further experimental dissection of the transcription regulatory landscape of CLL. For example, mCLL-associated regions were enriched for transcription factors that are active in mature B cells and involved in memory B cell differentiation (BATF, BCL6), whereas the uCLL group was enriched for regulatory regions that are active in other hematopoietic cell types, indicative of a less differentiated cell state. Moreover, pathways that may boost proliferation, such as NOTCH signaling [41] and interferon signaling [42], were specifically observed in the

more aggressive subtype (uCLL), whereas enrichment of inhibitory signaling by CTLA4 may contribute to the more indolent character of mCLL[43]. Beyond a small number of specific differences, the inferred gene regulatory networks were highly similar between mCLL and uCLL, consistent with the low number of differentially expressed genes that were previously observed between CLL subtypes[16,44,45].

From a technological perspective, our study describes broadly applicable methods for dissecting chromatin profiles in large cohorts of primary patient samples. The differential chromatin analysis outlined in Figure 3 starts from clinical and/or diagnostic data and uses supervised learning techniques to identify and cross-validate discriminatory chromatin signatures. We focused specifically on IGHV mutation status, but the method can be applied to any type of patient grouping, for example based on disease progression or therapy response. Moreover, the described method for ATAC-seq based inference of gene regulatory networks (Figure 4) establishes a data-driven approach for dissecting regulatory cell states – including their differences between disease subtypes – that is highly complementary to previous work aimed at inferring regulatory networks from transcriptome data[46,47,48]. Finally, the "chromatin accessibility corridor" (Figure 2) adapts a related concept[49] to provide intuitive browser-based visualization of chromatin data across large cohorts while accounting for regulatory heterogeneity. Relevant limitations of our study include: (i) Lack of a clearly defined and experimentally accessible cell-of-origin for uCLL and mCLL, making it difficult to distinguish with certainty between chromatin patterns that are CLL-specific and those that are derived from the cell-of-origin; (ii) clonal heterogeneity of CLL within patients, which would be experimentally addressable only with single-cell sequencing technologies[50,51] that are currently limited in their genome-wide coverage; (iii) lack of scalable methods for distinguishing between functional and non-functional transcription factor binding; and (iv) ambiguities in the assignment of transcription factor binding sites to the genes that they regulate. In the light of these limitations, the inferred gene regulatory networks constitute an initial model that will require future refinement as additional data and validations become available.

In summary, our study establishes a chromatin accessibility landscape of CLL, which identifies shared gene regulatory networks as well as widespread heterogeneity between individual patients and between disease subtypes. It also provides a resource that can act as a starting point for deeper dissection of chromatin regulation in CLL, identification of therapeutically relevant mechanisms, and eventual translation of relevant discoveries into clinical practice. Given that the chromatin profiling assays used here (ATAC-seq and ChIPmentation) are sufficiently fast and straightforward for use in a clinical sequencing laboratory, chromatin deregulation is becoming increasingly tractable as a promising source of biomarkers for stratified cancer therapy.

Methods

Sample acquisition and clinical data

All patients were diagnosed and treated at the Royal Bournemouth Hospital (UK) according to the revised guidelines of the International Workshop Chronic Lymphocytic Leukemia/National Cancer Institute (IWCLL/NCI). Patients were selected to reflect the clinical and biological heterogeneity of the disease. Sequential samples were included for a total of 24 patients. All samples contained more than 80% leukemic cells. Established chromosomal rearrangements were diagnosed by fluorescence in situ hybridization (Abbott Diagnostics; DakoCytomation) or multiple ligation dependent probe amplification using the MLPA P037 CLL-1 probemix (MRC Holland SALSA) according to the manufacturers' instructions. Chromosome analysis was performed and reported according to the International System for Human Cytogenetic Nomenclature. IGHV was sequenced as previously described[4], and a threshold of >98% germline homology was taken to define the unmutated subset[4]. The study was approved and overseen by the local ethics committee of the contributing institutions.

ATAC-seq

Accessible chromatin mapping was performed using the ATAC-seq method as previously described[25], with minor adaptations. In each experiment, 105 cells were washed once in 50 μl PBS, resuspended in 50 μl ATAC-seq lysis buffer (10 mM Tris-HCl, pH 7.4, 10 mM NaCl, 3 mM MgCl2, and 0.1% IGEPAL CA-630) and centrifuged for 10 min at 4°C. Upon centrifugation, the pellet was washed briefly in 50 μl MgCl2 buffer (10 mM Tris, pH 8.0, and 5 mM MgCl2) before incubating in the transposase reaction mix (12.5 μl 2x TD buffer, 2 μl transposase (Illumina) and 10.5 μl nuclease-free water) for 30 min at 37°C. After DNA purification with the MinElute kit, 1 μl of the eluted DNA was used in a qPCR reaction to estimate the optimum number of amplification cycles. Library amplification was followed by SPRI size selection to exclude fragments larger than 1,200 basepairs. DNA concentration was measured with a Qubit fluorometer (Life Technologies). Library amplification was performed using custom Nextera primers[25]. The libraries were sequenced by the Biomedical Sequencing Facility at CeMM using the Illumina HiSeq3000/4000 platform and the 25 basepair paired-end configuration.

RNA-seq

Total RNA was isolated using the AllPrep DNA/RNA Mini Kit (Qiagen). RNA amount was measured using Qubit 2.0 Fluorometric Quantitation (Life Technologies), and the RNA integrity number (RIN) was determined using Experion Automated Electrophoresis System (Bio-Rad). RNA-seq libraries were prepared using a Sciclone NGS Workstation (PerkinElmer) and a Zepyhr NGS Workstation (PerkinElmer) with the TruSeq Stranded mRNA LT sample preparation kit (Illumina). Library amount and quality were determined using Qubit 2.0 Fluorometric Quantitation (Life Technologies) and Experion Automated Electrophoresis System (Bio-Rad). The libraries were sequenced by the Biomedical Sequencing Facility at CeMM using the Illumina HiSeq 3000/4000 platform and the 50 basepair single-read configuration.

ChIPmentation

ChIPmentation was carried out as previously described[26], with minor adaptions. Briefly, cells were washed once with PBS and fixed with 1% paraformaldehyde in up to 1 ml PBS for 10 minutes at room temperature. Glycine was added to stop the reaction. Cells were collected at 500 x g for 10 minutes at 4°C (subsequent work was performed on ice and used cool buffers and solutions unless otherwise specified) and washed twice with up to 0.5 ml ice-cold PBS supplemented with 1 μM PMSF. The pellet was lysed in sonication buffer (10 mM Tris-HCl, pH 8.0, 1 mM EDTA, pH 8.0, 0.25% SDS, 1x protease inhibitors (Sigma), 1 μM PMSF) and sonicated with a Covaris S220 sonicator for 20-30 minutes in a milliTUBE or microTUBE until the size of most fragments was in the range of 200-700 basepairs. Lysates were centrifuged at full speed for 5 minutes at 4°C, and the supernatant containing the sonicated chromatin was transferred to a new tube. The lysate was then brought to RIPA buffer conditions (final concentration: 10 mM Tris-HCl, pH 8.0, 1 mM EDTA, pH 8.0, 140 mM NaCl, 1% Triton x-100, 0.1% SDS, 0.1% DOC, 1x protease inhibitors (Sigma), 1 μM PMSF) to a volume of 200 μl/immunoprecipitation. For each immunoprecipitation, 10 μl magnetic Protein A (Life Technologies) were washed twice and resuspended in PBS supplemented with 0.1% BSA. The antibody was added and bound to the beads by rotating 2 hours at 4°C. Used antibodies were H3K4me1 (0.5 μg/immunoprecipitation, Diagenode pAb-194-050), H3K27ac (1 μg/immunoprecipitation, Diagenode pAB-196-050), H3K27me3 (1 μg/immunoprecipitation, Millipore 07-499). For control libraries an IP with 2.5 μg of a nonspecific IgG rabbit antibody was used. Blocked antibody-conjugated beads were then placed on a magnet, supernatant was removed, and the

sonicated lysate was added to the beads followed by incubation for 3-4 hours at 4°C on a rotator. Beads were washed subsequently with RIPA (twice), RIPA-500 (10 mM Tris-HCl, pH 8.0, 1 mM EDTA, pH 8.0, 500 mM NaCl, 1% Triton x-100, 0.1% SDS, 0.1% DOC,) (twice), and RIPA-LiCl (10 mM Tris- HCl, pH 8.0, 1 mM EDTA, pH 8.0, 250 mM LiCl, 1% Triton X-100, 0.5% DOC, 0.5% NP40) (twice).

Beads were washed once with cold Tris-Cl pH 8.0 to remove detergent, salts, and EDTA. Beads were washed once more with cold Tris-Cl pH 8.0 but the reaction was not placed on a magnet to discard supernatant immediately. Instead, the whole reaction including beads was transferred to a new tube, and then placed on a magnet to remove supernatant to decrease background. Beads were then carefully resuspended in 25 μl of the tagmentation reaction mix (10 mM Tris pH 8.0, 5 mM MgCl2, 10% v/v dimethylformamide) containing 1 μl Tagment DNA Enzyme from the Nextera DNA Sample Prep Kit (Illumina) and incubated at 37°C for 1-3 minutes in a thermocycler. The beads were washed with RIPA (twice) and once with cold Tris-Cl pH 8. Beads were washed once more with cold Tris-Cl pH 8.0 but the reaction was not placed on a magnet to discard supernatant immediately. Instead, the whole reaction including beads was again transferred to a new tube, and then placed on a magnet to remove supernatant. Beads were then incubated with 70 μl elution buffer (0.5% SDS, 300 mM NaCl, 5 mM EDTA, 10 mM Tris-HCl pH 8.0) containing 2 μl of Proteinase K (NEB) for 1 hour at 55°C and 8 hours at 65°C to revert formaldehyde crosslinking, and supernatant was transferred to a new tube. Finally, DNA was purified with SPRI AMPure XP beads (sample-to-beads ratio 1:2) or Qiagen MinElute columns.

1 μl of each library was amplified in a 10-μl qPCR reaction containing 0.15 μM primers, 1× SYBR Green and 5 μl Kapa HiFi HotStart ReadyMix (Kapa Biosystems) to estimate the optimum number of enrichment cycles with the following program: 72°C for 5 min; 98°C for 30 s; 24 cycles of 98°C for 10 s, 63°C for 30 s; and 72°C for 30 s; and a final elongation at 72°C for 1 min. Kapa HiFi HotStart ReadyMix was incubated at 98°C for 45 s before preparation of all PCR reactions (qPCR and final enrichment PCR) to activate the hot-start enzyme for successful nick translation at 72°C in the first PCR step. Final enrichment of the libraries was performed in a 50 μl reaction using 0.75 μM primers and 25 μl Kapa HiFi HotStart ReadyMix. Libraries were amplified for N+1 cycles, where N is equal to the rounded-up Cq value determined in the qPCR reaction. Enriched libraries were purified using SPRI AMPure XP beads at a beads-to-sample ratio of 1:1, followed by a size selection using AMPure XP beads to recover libraries with a fragment length of 200-400 basepairs. Library preparation was performed using custom Nextera primers as described for ATAC-seq[25]. The libraries were sequenced by the Biomedical Sequencing Facility at CeMM using the Illumina HiSeq3000/4000 platform and the 25 basepair paired-end configuration.

Processing of the ATAC-seq data

Reads were trimmed using Skewer[52]. Trimmed reads were aligned to the GRCh37/hg19 assembly of the human genome using Bowtie2[53] with the "-very-sensitive" parameter. Duplicate reads were removed using sambamba markdup[54], and only properly paired reads with mapping quality >30 and alignment to the nuclear genome were kept. All downstream analyses were performed on the filtered reads. Genome browser tracks were created with the genomeCoverageBed command in BEDTools[55] and normalized such that each value represents the read count per basepair per million mapped and filtered reads. Finally, the UCSC Genome Browser's bedGraphToBigWig tool was used to produce a bigWig file. Combined tracks with percentile signal across the cohort were created by quantifying ATAC-seq read coverage at every reference genome position using BEDTools coverage and normalizing it between samples. Normalization was done by dividing each value by the total number of filtered reads and multiplying it with 10 million, in order to obtain numbers that are comparable and easy to visualize. Next, the mean as well as the 5th, 25th, 75th and 95th percentiles of signal across the whole cohort were calculated with Numpy, converted into bedgraph files, and subsequently to bigwig format using bedGraphToBigWig. Peak calling was

performed with MACS2[56] using the "-nomodel" and "-extsize 147" parameters, and peaks overlapping blacklisted features as defined by the ENCODE project[57] were discarded.

Preprocessing of the RNA-seq data

Reads were trimmed with Trimmomatic[58] and aligned to the GRCh37/hg19 assembly of the human genome using Bowtie1[59] with the following parameters: -q -p 6 -a -m 100 –minins 0 –maxins 5000 –fr –sam –chunkmbs 200. Duplicate reads were removed with Picard's MarkDuplicates utility with standard parameters prior to transcript quantification with BitSeq[60] using the Markov chain Monte Carlo method and standard parameters. To obtain gene-level quantifications, we assigned the expression values of its highest expressed transcript to each gene. Differential gene-level expression between the three IGHV mutation status groups was performed using DESeq2[61] from the raw count data with a significance threshold of 0.05. To produce genome browser tracks, we mapped the reads to the genomic sequence of the GRCh37/hg19 assembly of the human genome using Bowtie2[53] with the "-very-sensitive" parameter, removed duplicates using sambamba markdup[54], and used the genomeCoverageBed command in BEDTools[55] to produce a bedgraph file. This file was normalized such that each value represents the read count per basepair per million filtered reads, and the UCSC Genome Browser's bedGraphToBigWig tool was used to convert it into a bigWig file.

Preprocessing of the ChIPmentation data

Reads were trimmed using Skewer[52]. Trimmed reads were aligned to the GRCh37/hg19 assembly of the human genome using Bowtie2[53] with the "-very-sensitive" parameter. Duplicate reads were removed using sambamba markdup[54], and only properly paired reads with mapping quality >30 and alignment to the nuclear genome were kept. All downstream analyses were performed on the filtered reads. Genome browser tracks were created with the genomeCoverageBed command in BEDTools[55] and normalized such that each value represents the read count per basepair per million filtered reads. Finally, the UCSC Genome Browser's bedGraphToBigWig tool was used to produce a bigWig file.

Bioinformatic analysis of chromatin accessibility

The CLL consensus map was created by merging the ATAC-seq peaks from all samples using the BEDTools[55] merge command. To produce Figure 1b, we counted the number of unique chromatin-accessible regions after merging peaks for each sample in an iterative fashion, randomizing the sample order 1,000 times and computing 95% confidence intervals across all iterations. The chromatin accessibility of each region in each sample was quantified using Pysam, counting the number of reads from the filtered BAM file that overlapped each region. To normalize read counts across samples, we performed quantile normalization using the normalize.quantiles function from the preprocessCore package in R. For each genomic region we calculated the support as the percentage of samples with a called peak in the region, and we calculated four measures of ATAC-seq signal variation across the cohort: mean signal, standard deviation, variance-to-mean ratio, and the squared coefficient of variation (the square of the standard deviation over the mean). Additionally, we used BEDTools intersect to annotate each region with the identity of and distance to the nearest transcription start site and the overlap with Ensembl gene annotations (promoters were defined as the 2,500 basepair region upstream of the transcription start site).

Annotation with chromatin states was based on the 15-state genome segmentation for CD19+ B cells from the Roadmap Epigenomics Project[62] (identifier: E032).

To summarize the chromatin accessibility signals into one value per gene (Figure 2b and Supplementary Figure 5) we used the accessibility values of the closest region (but no further than 1,000 basepairs from the transcription start site) to represent the promoter, and the mean values of all distal regions (located more than 2,500 basepairs from the transcription start site) of each gene to represent distal regulatory elements. To test for overrepresentation of CpG islands in the promoters of genes with a known role in B cell biology and/or CLL pathogenesis, we downloaded the position of CpG islands in the GRCh37/hg19 assembly from the UCSC Genome Browser[63], counted the number of promoters (as defined above) that overlapped by at least one basepair with CpG islands in the gene set of interest and in all other genes with accessible elements in CLL, and used Fisher's exact test to assess the significance of the association. Unsupervised principal component analysis was performed with the scikit-learn[64] library (sklearn.decomposition.PCA) applied to the chromatin accessibility values of all chromatin-accessible regions across the CLL cohort.

To investigate variability within the mCLL and uCLL sample groups, we divided the samples in two groups based on their IGHV mutation status (samples below a 98% homology threshold were considered mutated and samples with missing values for the IGHV mutation status were excluded from the analysis), and we used the F test from the var.test function in R on the chromatin accessibility values of all CLL cohort regions. Significantly variable regions were defined as having a Bonferroni-corrected p-value below 0.05 and mean accessibility above 1. Region set enrichment analysis was performed on the significantly variable regions of each group using LOLA[31] with its core databases: transcription factor binding sites from ENCODE[57], tissue clustered DNase hypersensitive sites[65], the CODEX database{Sanchez-Castillo, 2015 }, UCSC Genome Browser annotation tracks[63], the Cistrome database[66], and data from the BLUEPRINT project[67]. Motif enrichment analysis was performed with the AME tool from the MEME suite[68] using 250 basepair sequences centered on the chromatin-accessible regions and randomly generated sequences of the same length and set size from a distribution of 0th and 1st order Markov order (single nucleotides and dinucleotide) frequencies as background.

Machine learning analysis of disease subtypes

Random forest classifiers from the scikit-learn[64] Python library (sklearn.ensemble.RandomForestClassifier) were trained with the samples' IGHV mutation status as class label and the chromatin accessibility values for each sample at each of the 112,298 consensus regions as input features (prediction attributes). All samples with known IGHV mutation status were used for class prediction, the performance was evaluated by leave-one-out cross-validation, and the results were plotted as ROC curves using scikit-learn. Given that several patients contributed more than one sample to the cohort, in each iteration of the cross-validation we removed any samples from the training set that belonged to the same patient as the sample in the test set, in order to eliminate a potential risk of overtraining. Furthermore, we repeated the cross-validation 1,000 times based on randomly shuffled class labels to confirm that no overtraining occurred in our analysis. The most predictive regions for IGHV mutation status were selected by averaging the feature importance of the random forest classifiers over all iterations of the cross-validation and selecting those features with Gini importance higher than 10-4. Region set enrichment was performed using LOLA[31] as described above. Pathway enrichment analysis was performed using seq2pathway[69]. The sample clustering in Figure 4a was based on the pairwise correlation of ATAC-seq signal in the predictive regions between samples, and the dendrogram was plotted using Scipy's hierarchical clustering function. With the same values of chromatin accessibility from above, we performed principal component analysis on the CLL samples using R's implementation in the prcomp function. To provide further validation of the machine learning analysis, we also identified differential ATAC-seq peaks between IGHV mutated and

IGHV unmutated samples using the DESeq2 R package[61]. This statistical analysis was based on read counts for all CLL-accessible regions in each patient, testing for differential chromatin accessibility using a model based on the negative binomial distribution. Regions with Benjamini-Hochberg adjusted p-values below 0.01 and an absolute log2 fold-change above 1 were used for the comparison with those signature regions identified by the machine learning analysis.

Gene regulatory network inference

Transcription factor binding maps as the basis for inferring gene regulatory networks were derived by footprinting analysis using the PIQ software[70] and a set of 366 human transcription factor motifs from the JASPAR database[38]. We retained only those transcription factors with at least 500 high-purity (>0.7) binding sites overlapping with an ATAC-seq peak, as previously described[71]. Binding sites located in the gene body or in the 2,500 basepair region upstream of its transcription start site were assigned to the overlapping gene(s), and intergenic binding sites were assigned to the gene whose transcription start site was closest to the peak. This assignment was based on the Ensembl gene annotation version 75, and we treated non-protein-coding genes in the same way as protein-coding genes. To infer gene regulatory networks, an interaction score was calculated in a similar way as previously described[71]: The interaction score between a transcription factor t and a gene g (St,g) was defined as the sum over all n transcription factor binding sites of t that can be assigned to g:

$$S_{t,g} = \sum_{i=0}^{n} 2 \times (P_i - 0.5) * 10^{-(\frac{d_{i,g}}{100000})} \quad (1)$$

In this formula Pi is the PIQ purity score and di,g is the distance of a particular transcription factor binding site i to gene g. This score establishes a unidirectional (transcription factors to genes) and weighted (based on the interaction score) relationship, providing the edges of the gene regulatory network. We inferred gene regulatory networks for all samples combined and also separately for the two disease subtypes (mCLL and uCLL) based on IGHV mutation status. We considered only transcription-factor-to-gene interactions with scores above 1, and in Figure 5b as well as Supplementary Figures 17 and 19 we plotted only nodes with more than 200 connections. For the CD19+ B cell gene regulatory network we used DNase-seq data from the Roadmap Epigenomics Project[62] (identifier: E032). Both the processing of the raw data and the network inference were performed in the same manner as for ATAC-seq. The comparison of composition and structural characteristics of the gene regulatory networks inferred from ATAC-seq data for the CLL cohort and from DNase-seq data for CD19+ B cells was done using functions from the networkx[72] library in Python. The inferred networks were visualized using the Gephi software, applying the Force Atlas 2 graph layout with LinLog and hub dissuasion. In order to compare the inferred mCLL and uCLL networks, we divided the degree of each node by the total number of edges in each network to compensate for differences in the absolute number of detected interactions, and we quantified differences by subtracting and log2-transforming this value between networks for each node.

Data availability

All data are available as genome browser tracks for interactive browsing and download from the supplementary website (http://cll-chromatin.computational-epigenetics.org/). The processed data are also openly available from NCBI GEO (accession number pending, will be added at proof stage), whereas the raw sequencing data are available from EBI EGA (accession number pending, will be added at proof stage) under a controlled access regimen to protect the privacy of the patients who have donated the samples.

Acknowledgements

We would like to thank all patients who have donated their samples for this study. We also thank Amelie Kuchler and Thomas Penz for expert technical assistance, Johanna Klughammer and Nathan Sheffield for their contributions to the data analysis pipeline, the Biomedical Sequencing Facility at CeMM for assistance with next-generation sequencing, and all members of the Bock lab for their help and advice. Moreover, we would like to thank Ulrich Jäger, Medhat Shehata, Philipp Staber, and Jörg Menche for their comments and for critically reading the manuscript. This work was performed in the context of the BLUEPRINT project (European Union's Seventh Framework Programme grant agreement no. 282510) and the ERA-NET projects EpiMark (FWF grant agreement no. I 1575-B19) and CINOCA (FWF grant agreement no. I 1626-B22). C.S. was supported by a Feodor Lynen Fellowship of the Alexander von Humboldt Foundation. J.C.S. was supported by Bloodwise (11052, 12036), the Kay Kendall Leukaemia Fund (873), Cancer Research UK (C34999/A18087, ECMC C24563/A15581), Wessex Medical Research, and the Bournemouth Leukaemia Fund. C.B. was supported by a New Frontiers Group award of the Austrian Academy of Sciences.

Author contributions

A.F.R., C.S., J.C.S., D.O., and C.B. planned the study; J.C.S., R.W., Z.D., and D.O. provided samples and clinical data; C.S. and M.F. performed the experiments; A.F.R. analyzed the data with contributions from C.S., J.C.S., D.O., and C.B.; C.B. supervised the research; all authors contributed to the writing of the manuscript.

Competing financial interests

The authors declare no competing financial interests.

Figures

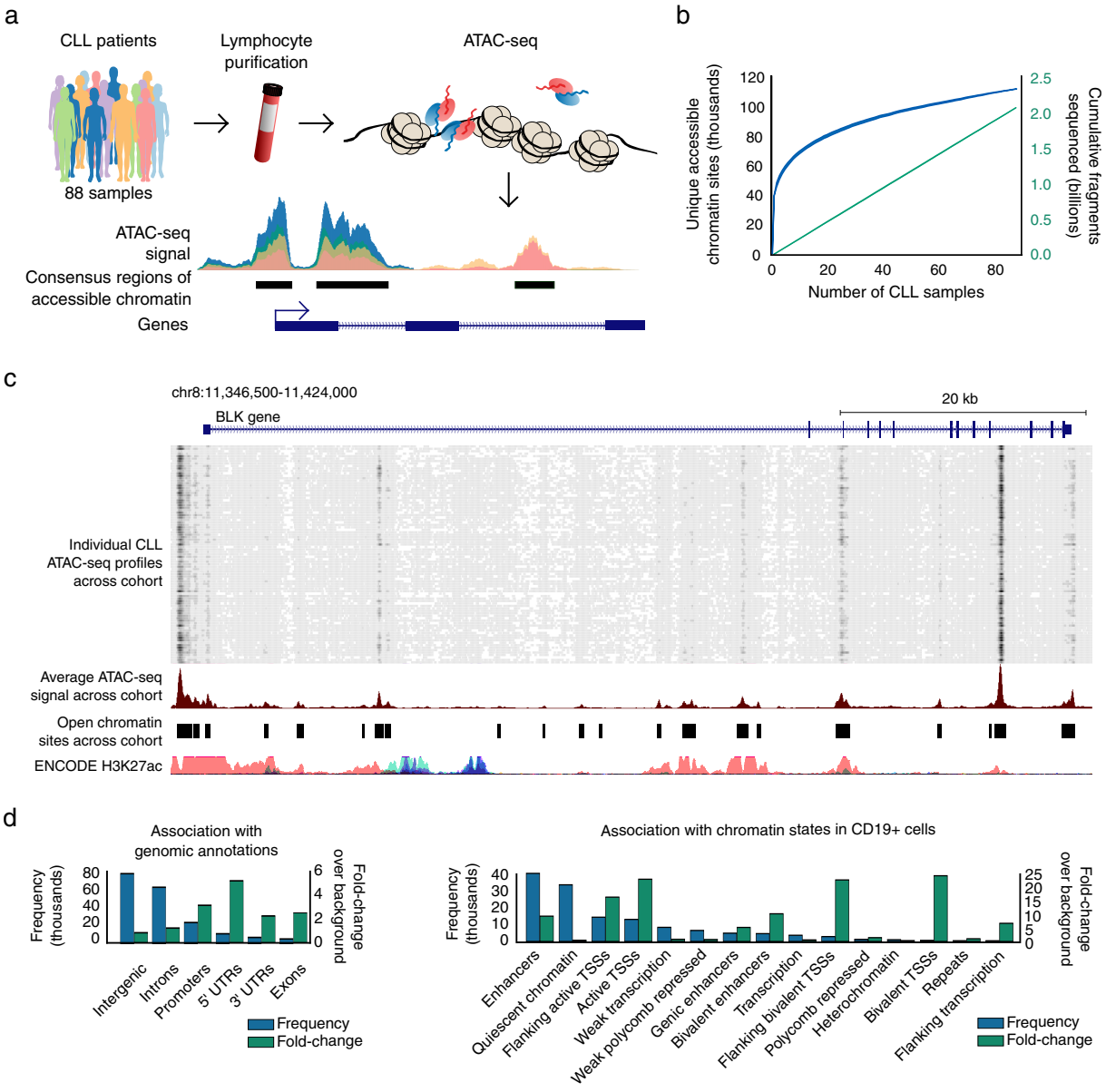

Figure 1. *The chromatin accessibility landscape of chronic lymphocytic leukemia (CLL).* **a)** ATAC-seq profiling and analysis workflow for establishing patient-specific and cohort-level maps of chromatin accessibility in CLL. **b)** Saturation analysis showing the number of unique chromatin-accessible regions detected across 88 samples and with a total sequencing depth of 2.2 billion ATAC-seq fragments. The narrow blue and green corridors indicate 95% confidence intervals for samples added in random order (1,000 iterations). **c)** Genome browser plot showing ATAC-seq signal intensity for 88 individual CLL samples (top), average signal intensity across the cohort and cohort-level peak calls (center), and reference data from the ENCODE project (bottom). Interactive genome browser tracks are available from the supplementary website: http://cll-chromatin.computational-epigenetics.org/. **d)** Absolute (frequency) and relative (fold-change) co-localization of unique chromatin-accessible regions in CLL with gene annotations (left) and chromatin state segmentations for CD19+ B cells from the Roadmap Epigenomics project (right).

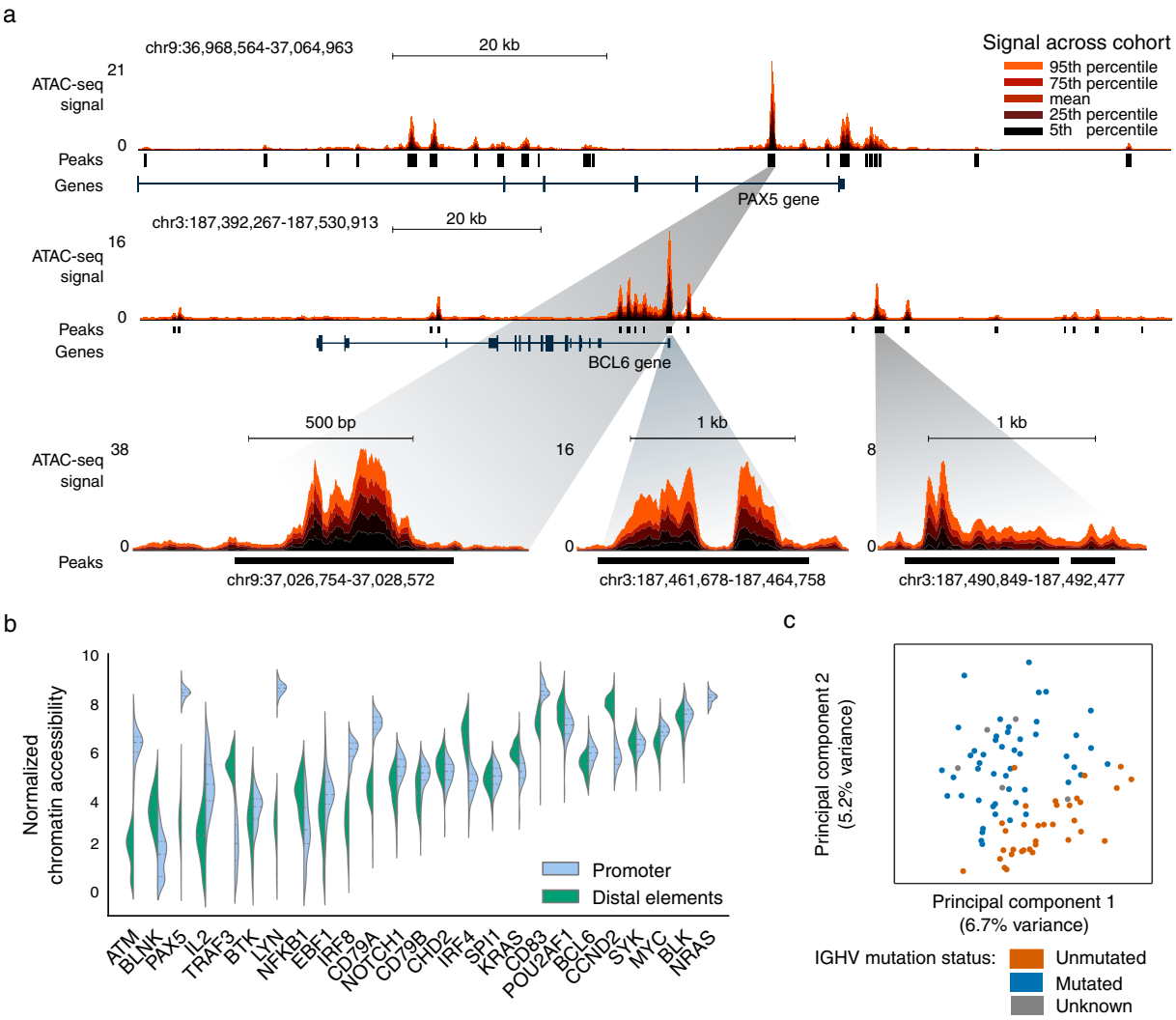

Figure 2. *Heterogeneity in the CLL chromatin accessibility landscape.* **a)** Genome browser plot showing ATAC-seq signal intensity across the CLL cohort in the vicinity of two genes with a known role in B cell biology (PAX5 and BCL6). This cohort-level track uses color-coded percentiles to visualize the observed heterogeneity between samples. The bottom row zooms in on the chromatin accessibility landscape at three specific regulatory regions. **b)** Violin plots showing the cohort-wide distribution of chromatin accessibility at promoters (chromatin-accessible regions located with 2,500 basepairs from the transcription start site) and putative enhancers of genes with a known role in B cell biology and/or CLL pathogenesis. **c)** Unsupervised principal component analysis based on the chromatin accessibility for all 88 samples at each of the 112,298 chromatin-accessible regions in the CLL cohort. Samples are color-coded according to their IGHV mutation status, using $< 98\%$ germline homology as threshold for classifying a sample as mutated.

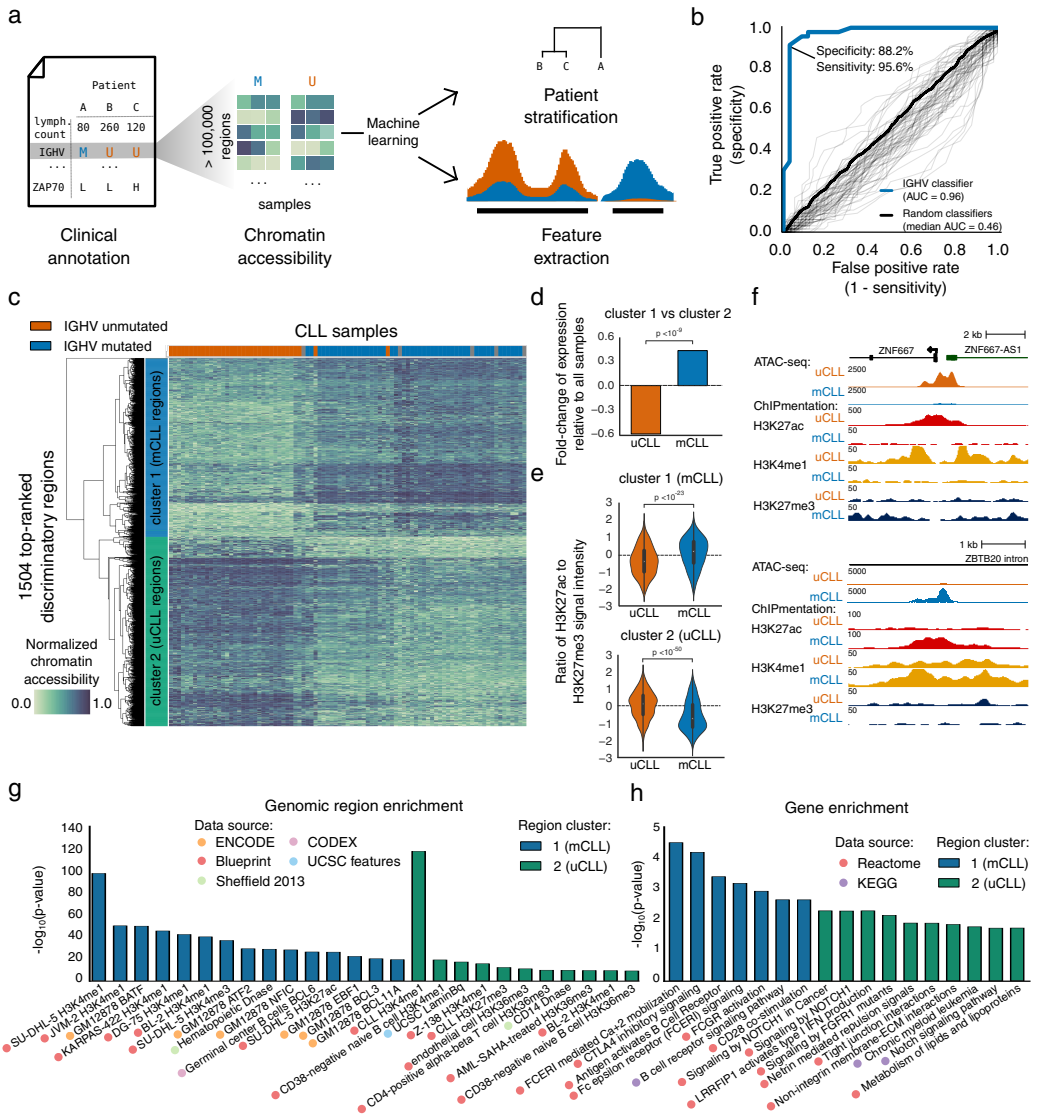

Figure 3. *Disease subtype-specific patterns of chromatin accessibility.* **a)** Methodology for deriving disease subtype-specific patterns of chromatin accessibility: A machine learning algorithm is trained to distinguish between different sample sets (here: IGHV-mutated vs. IGHV-unmutated), the prediction performance is evaluated by cross-validation, and the most predictive features are obtained by feature extraction from the trained classifiers. **b)** ROC curve summarizing the test set prediction performance (estimated by leave-one-out cross-validation) of a random forest classifier that uses the ATAC-seq dataset to distinguish between IGHV-mutated and IGHV-unmutated samples. "AUC" refers to the ROC area under curve as a measure of prediction performance, and sensitivity/specificity values are shown for the point on the ROC curve that is closest to the top left corner. The grey lines indicate the performance of 1,000 classifiers trained and evaluated in the same way but based on randomly shuffled class labels. **c)** Clustered heatmap based on the most predictive regions extracted from the cross-validated classifiers. **d)** Ratio of expression levels for genes linked to mCLL-accessible regions vs. genes linked to uCLL-accessible regions. **e)** Ratio between ChIPmentation signal for active chromatin (H3K27ac) and repressive chromatin (H3K27me3) at mCLL-linked and uCLL-linked regions. **f)** Genome browser plots showing ATAC-seq and ChIPmentation profiles for gene loci with a known role in CLL (ZNF667 and ZBTB20). **g)** Most highly enriched region sets for mCLL (blue) and uCLL (green) associated regions. **h)** Most highly enriched pathways among genes linked to mCLL (blue) and uCLL (green) regions.

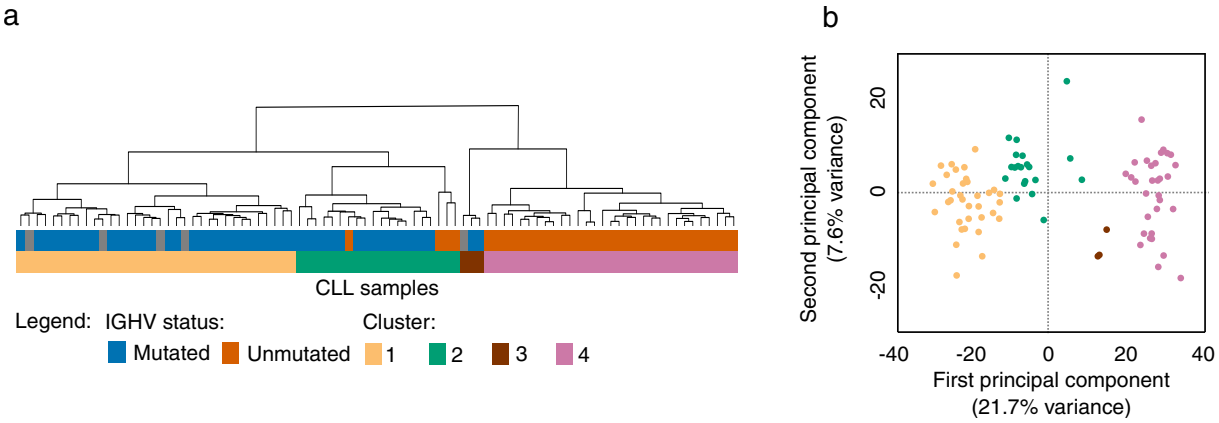

Figure 4. *Patient stratification into CLL subtypes based on chromatin accessibility.* **a)** Hierarchical clustering of all CLL samples based the classifiers' most predictive regions. Clusters 1 corresponds to mCLL, cluster 4 to uCLL, and the clusters 2 and 3 correspond to iCLL. Samples are colored by IGHV mutation status (top) and cluster assignment (bottom). **b)** Principal component analysis for the same data as in panel a, showing the first two principal components as well as their explained variance.

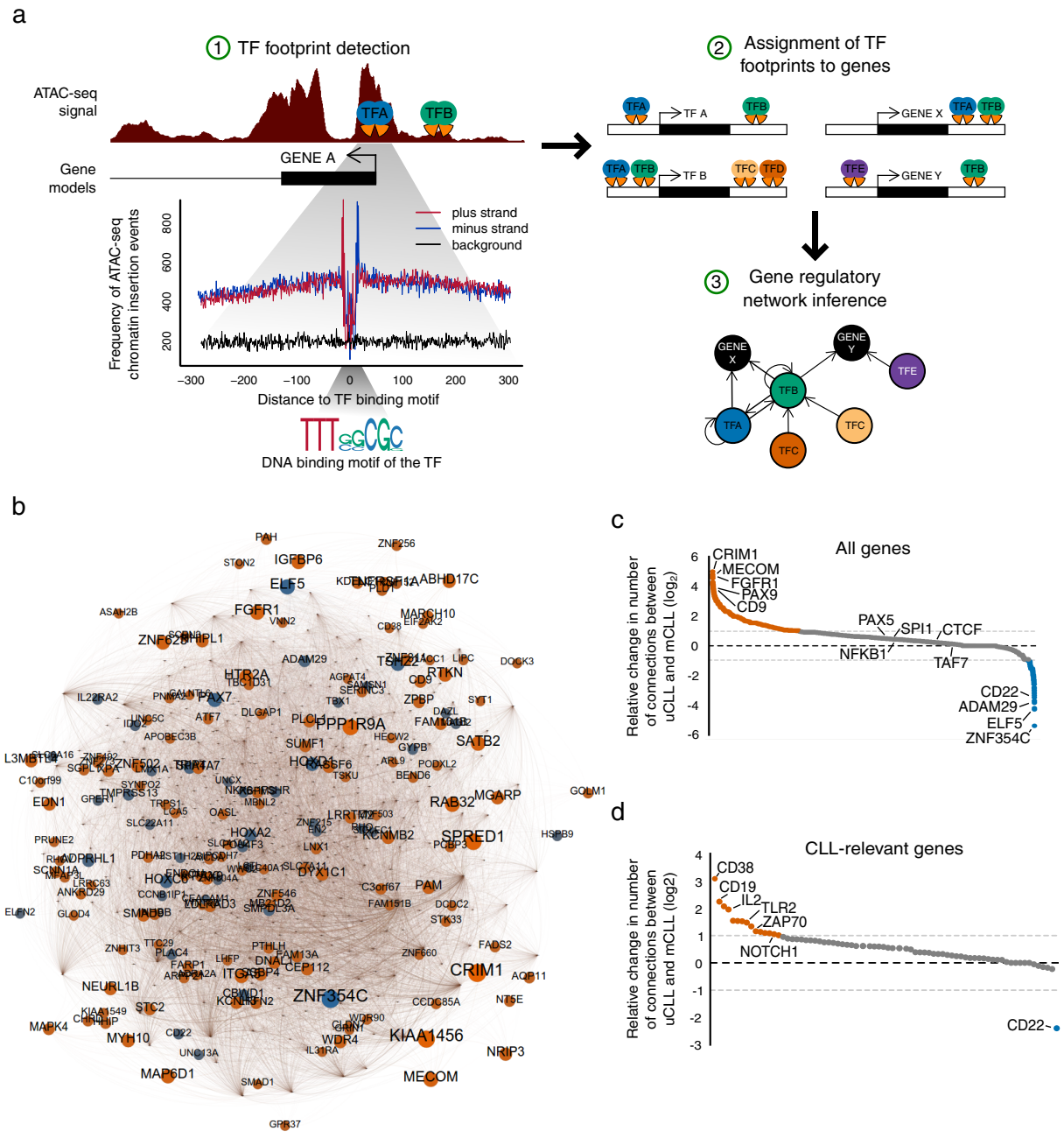

Figure 5. *Gene regulatory networks underlying the mCLL and uCLL disease subtypes.* **a)** Methodology for deriving gene regulatory networks from ATAC-seq data using transcription factor (TF) footprinting, mapping of transcription factor binding footprints to co-localized genes, and regulatory network inference. **b)** CLL gene regulatory network derived from the data of all 88 samples, showing the most differentially connected genes between uCLL and mCLL (the full network is shown in Supplementary Figure 18). Node size reflects the total number of connections of each node, and colors denote the subtype-specific network in which the nodes are more highly connected (mCLL: blue; uCLL: orange). **c)** Relative change in the number of connections between the mCLL and uCLL networks, showing all genes. **d)** Relative change in the number of connections between the mCLL and uCLL networks, focusing on genes with a known role in B cell biology and/or CLL pathogenesis.

Supplemental Data

Supplementary Data 1: Clinical annotations of the CLL patient cohort.

Clinical annotations for the patient samples that were analyzed in this study. All patients were diagnosed and treated at the Royal Bournemouth Hospital (UK).

Supplementary Data 2: Summary statistics of the sequencing experiments.

Sequencing statistics for 88 samples with ATAC-seq, 10 samples with ChIPmentation for three histone marks (H3K4me1, H3K27ac, H3K27me3) and one control (IgG), and 10 samples with RNA-seq.

Supplementary Data 3: Differentially expressed genes between CLL subtypes.

List of differentially expressed genes between three disease subtypes (mCLL, iCLL, uCLL), based on RNA-seq data for representative samples in each subtype.

Supplementary Data 4: Chromatin-accessible regions associated with IGHV mutation status.

List of regions with differential chromatin accessibility between IGHV-mutated and IGHV-unmutated CLL samples, based on the machine learning analysis or alternatively based on differential peak analysis using DESeq2.

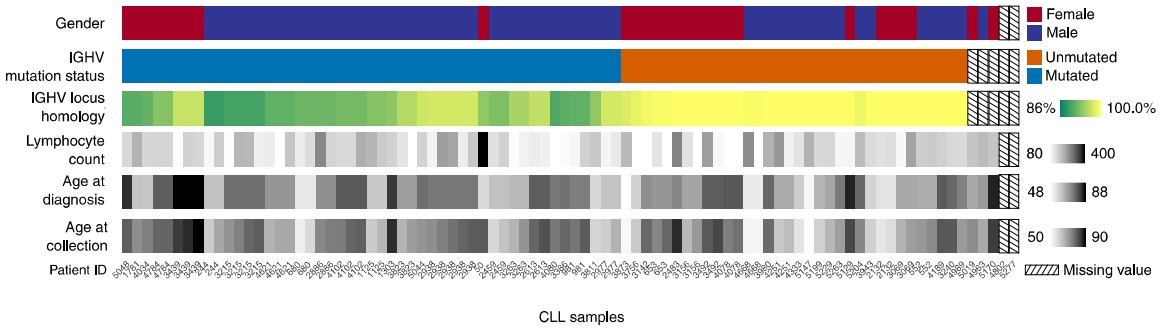

Supplementary Figure 1

The cohort reflects the spectrum of CLL phenotypes commonly encountered in clinical care.

Visualization of clinical annotations for the patient samples included in this study.

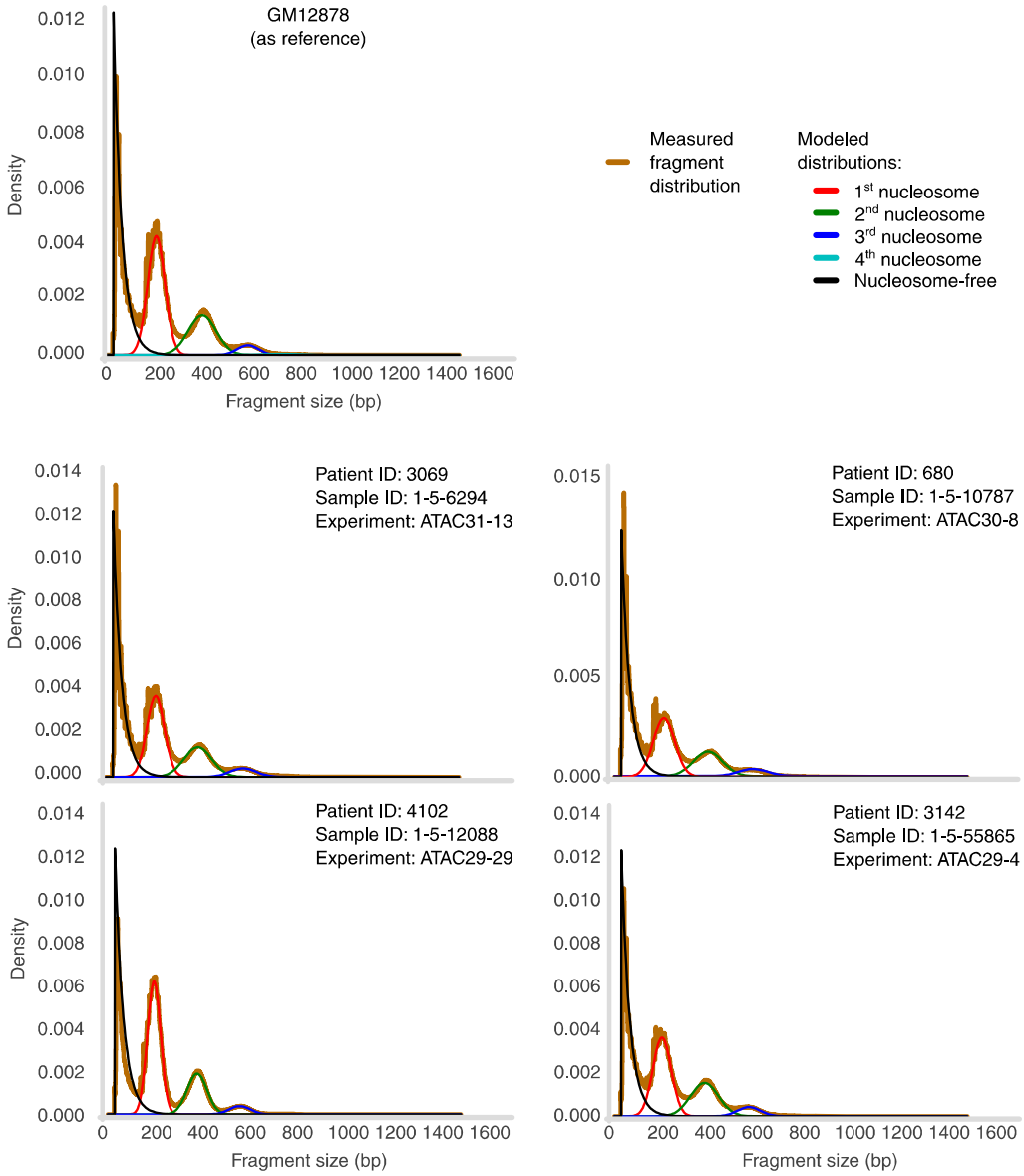

Supplementary Figure 2

Observed ATAC-seq fragment length distributions indicate high data quality.

Distribution of ATAC-seq fragment lengths for published GM12878 data (Buenrostro et al. 2013 Nature Methods) and for four randomly selected CLL samples from this study. Fragment lengths were inferred based on paired-end sequencing data. The characteristic patterns of nucleosome-associated fragment length are observed in all samples.

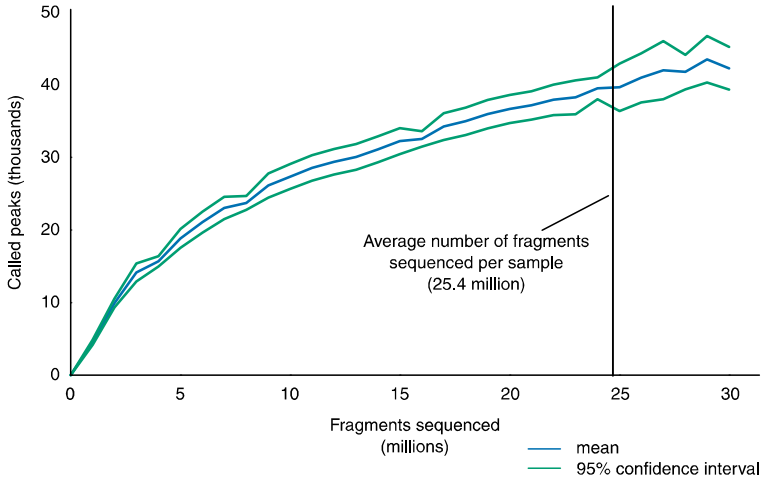

Supplementary Figure 3

The chosen sequencing depth recovers the majority of ATAC peaks per sample.

Relationship of the number of sequenced reads (x-axis) and the number of detected chromatin-accessible regions (y-axis), showing the average pattern across all 88 samples (blue line). The corridor indicated in green corresponds to a 95% confidence interval for random subsampling across samples.

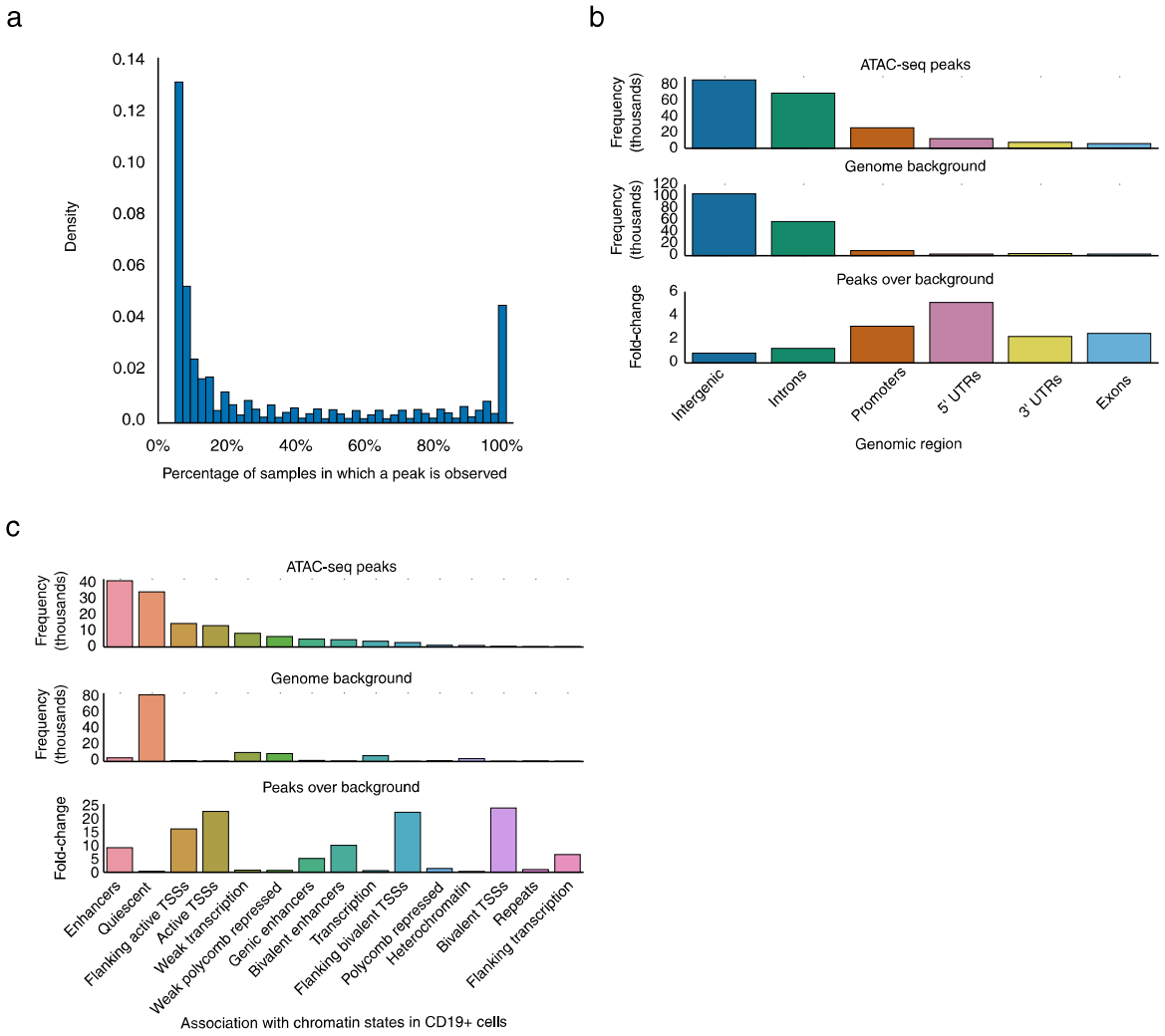

Supplementary Figure 4

Chromatin-accessible regions in CLL are enriched for promoters and enhancers.

a) Histogram showing the number of samples in which a given chromatin-accessible region from the CLL consensus map was detected as a significant ATAC-seq peak. b) Frequency of overlap and enrichment of Ensembl gene annotation for regions in the CLL consensus map, compared to region sets of identical size and lengths that were randomized 1,000 times across the genome. c) Frequency of overlap and enrichment of chromatin state segmentations for CD19+ B cells (data from the Roadmap Epigenomics project), compared to region sets of identical size and lengths that were randomized 1,000 times across the genome.

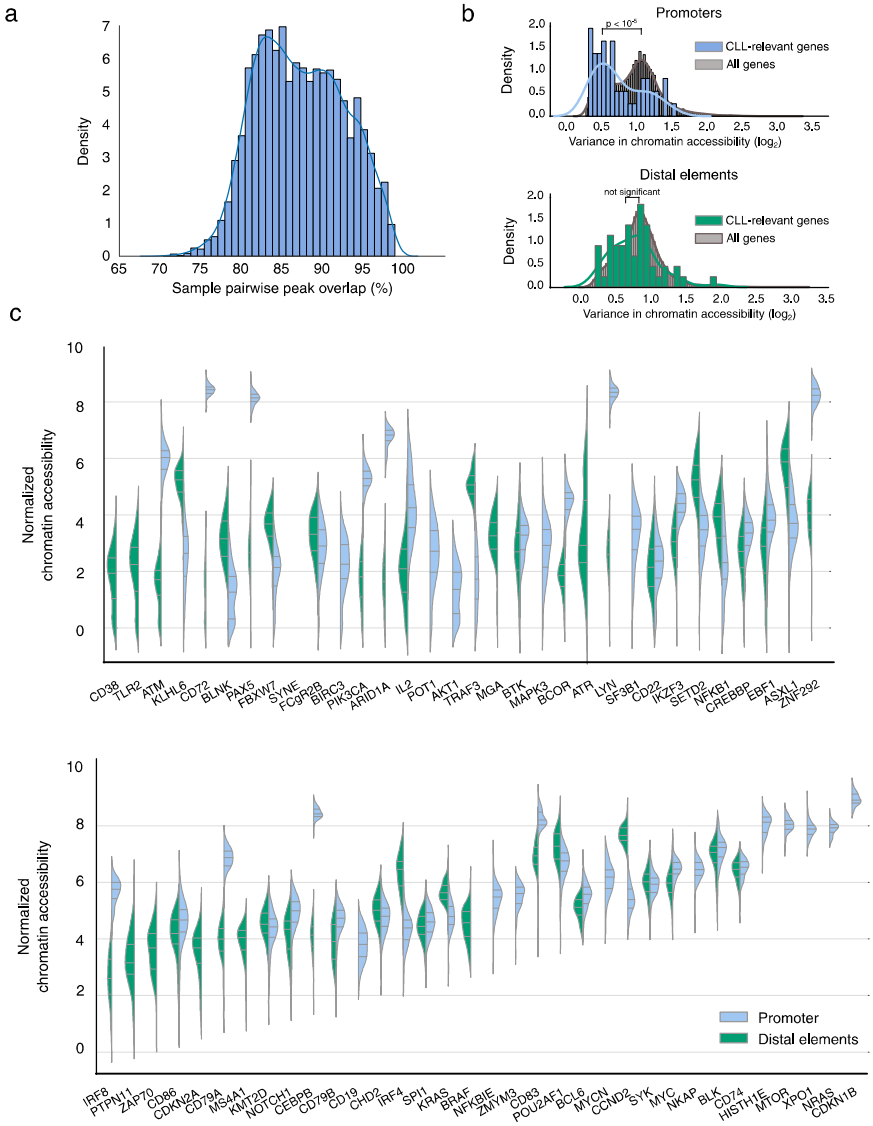

Supplementary Figure 5

Heterogeneity in chromatin accessibility affects genes related to B cells and CLL.

a) Histogram showing the percentage of chromatin-accessible regions that are shared between any two CLL samples. b) Distribution of variance in chromatin accessibility for promoter regions and putative distal regulatory regions across all genes (grey) and for a set of genes with a known role in B cell biology and/or CLL pathogenesis (blue/green). Chromatin accessibility scores were averaged across all regulatory regions assigned to a given gene. c) Violin plots of normalized chromatin accessibility values for gene promoters (regions located within 2,500 basepairs of the transcription start site) and distal regulatory elements (regions located at least 2,500 basepairs away from the nearest transcription start site) for the same genes as in panel b.

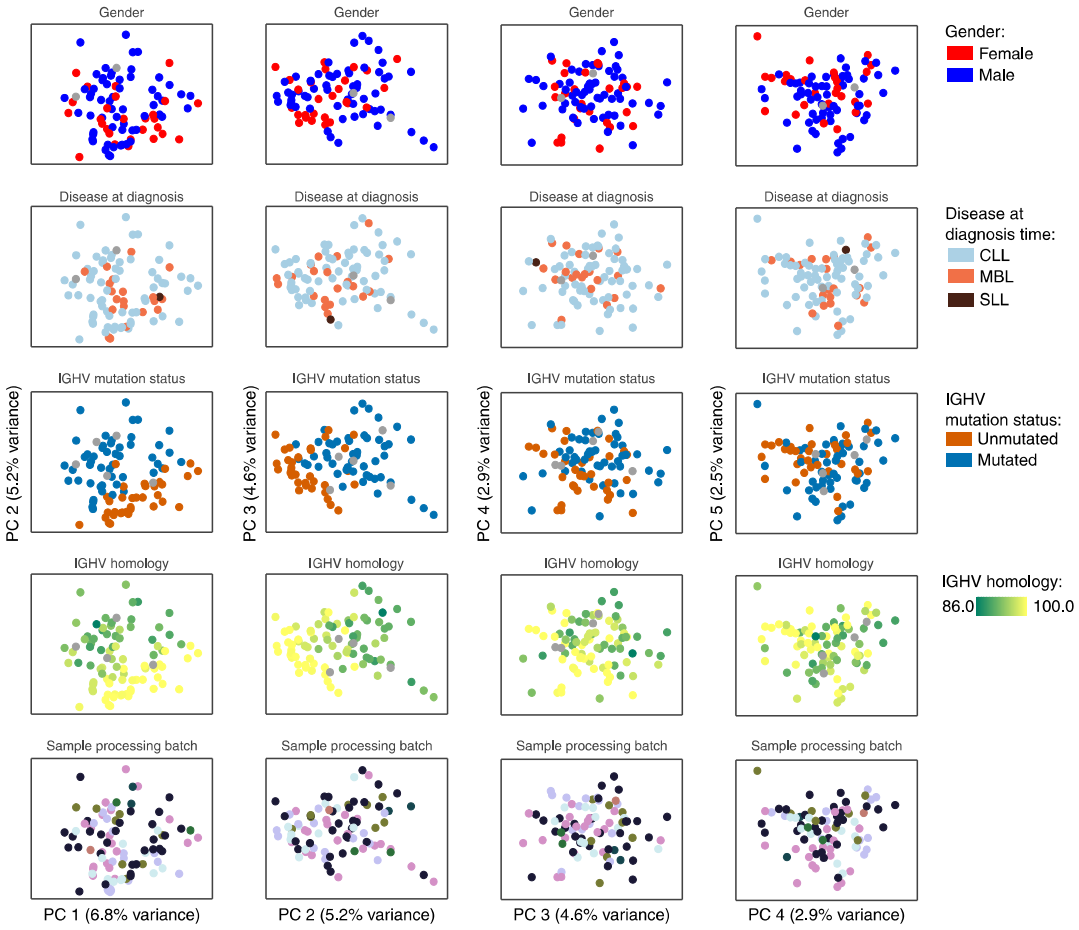

Supplementary Figure 6

Unsupervised analysis identifies IGHV mutation status as a key source of variation.

Principal component analysis based on the chromatin accessibility for all 88 samples at each of the 112,298 chromatin-accessible regions in the CLL cohort. The first five principal components are plotted, and samples are colored according to clinical annotations and molecular diagnostics data (top four rows) as well as the sample processing batch for the ATAC-seq experiments (bottom row).

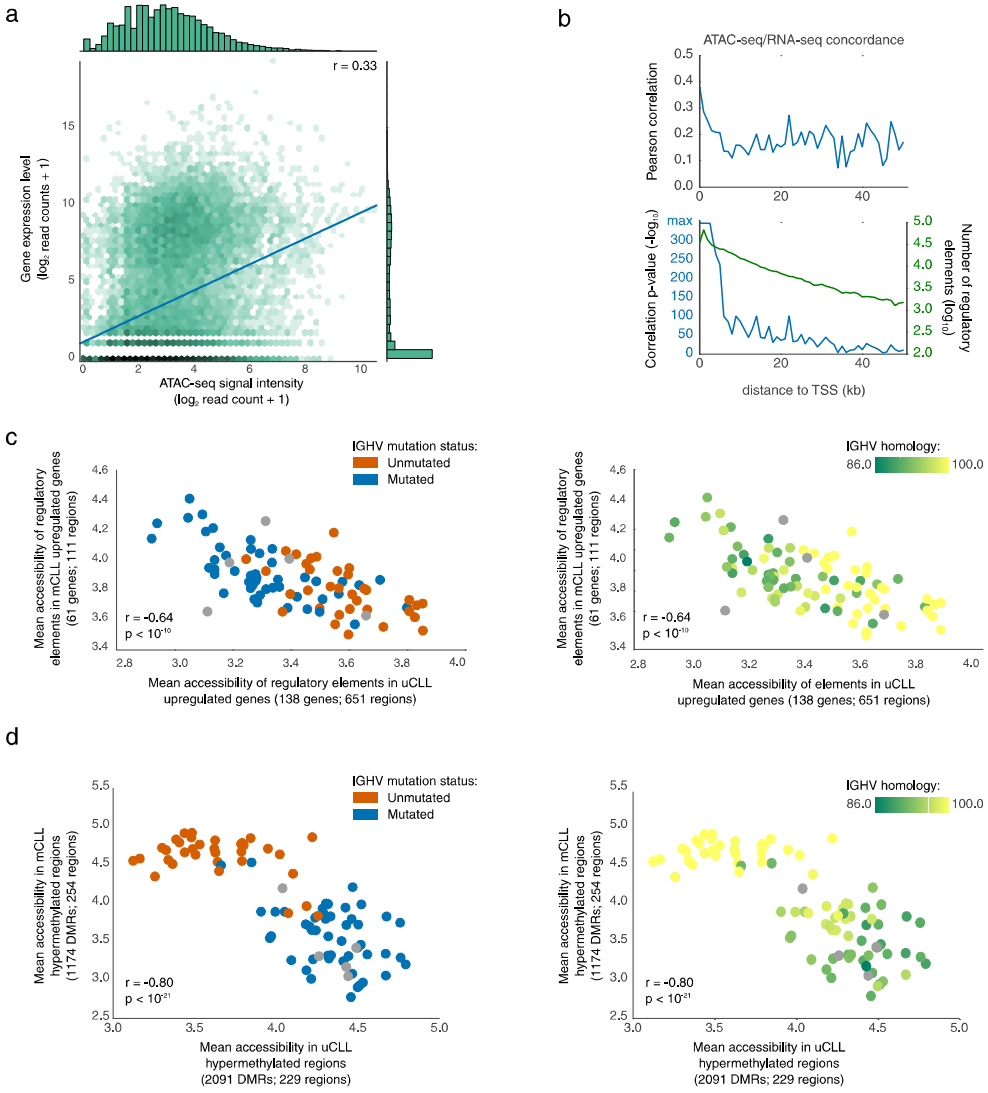

Supplementary Figure 7

Chromatin accessibility is linked to differences in gene expression and DNA methylation.

a) Hexbin scatterplot visualizing the weak correlation (Pearson's $r = 0.33$) between gene expression levels and the chromatin accessibility at associated regulatory regions. Shown are averages across ten samples with matched ATAC-seq and RNA-seq data. The color gradient is on a logarithmic scale. b) Pearson correlation (top) and significance of the association (bottom) between gene expression levels and chromatin accessibility values at associated regulatory regions, plotted over the distance of the accessible region to the gene's transcription start site. c) Mean chromatin accessibility across CLL-accessible regions associated with genes that were upregulated in *IGHV*-mutated or in *IGHV*-unmutated CLL. d) Mean chromatin accessibility in CLL-accessible regions that overlap with regions described as hypermethylated in *IGHV*-mutated or in *IGHV*-unmutated CLL (Kulis et al. 2012 Nature Genetics).

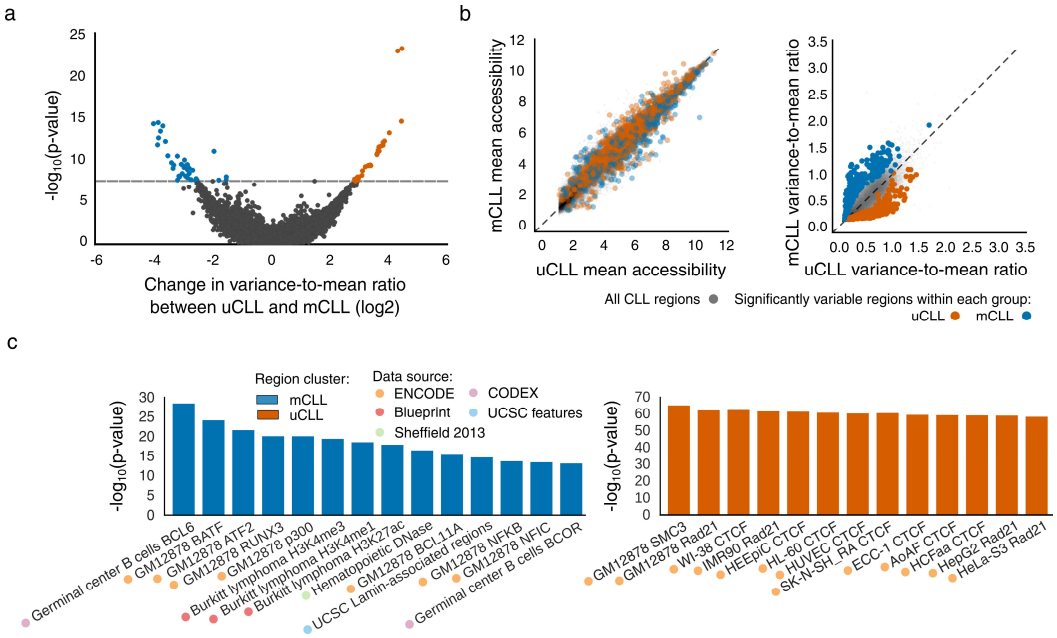

Supplementary Figure 8

Subtype-specific variable regions show characteristic enrichment patterns.

a) Differential variability between the mCLL and uCLL sample groups illustrated by each region's change in variance-to-mean ratio between groups (x-axis) and the *p*-value for variability within each group (y-axis). Blue and orange dots indicate significantly variable regions. b) Scatterplots of mean accessibility (left) and variance-to-mean ratio within each sample group (right). The plot on the left illustrates how significantly variable regions are dispersed across the accessibility range, rather than being strongly associated with differences in mean accessibility between the groups. The color coding is the same as in panel a. c) Most highly enriched region sets that significantly overlap with the differentially variable regions for mCLL (blue) and for uCLL (orange), based on LOLA analysis.

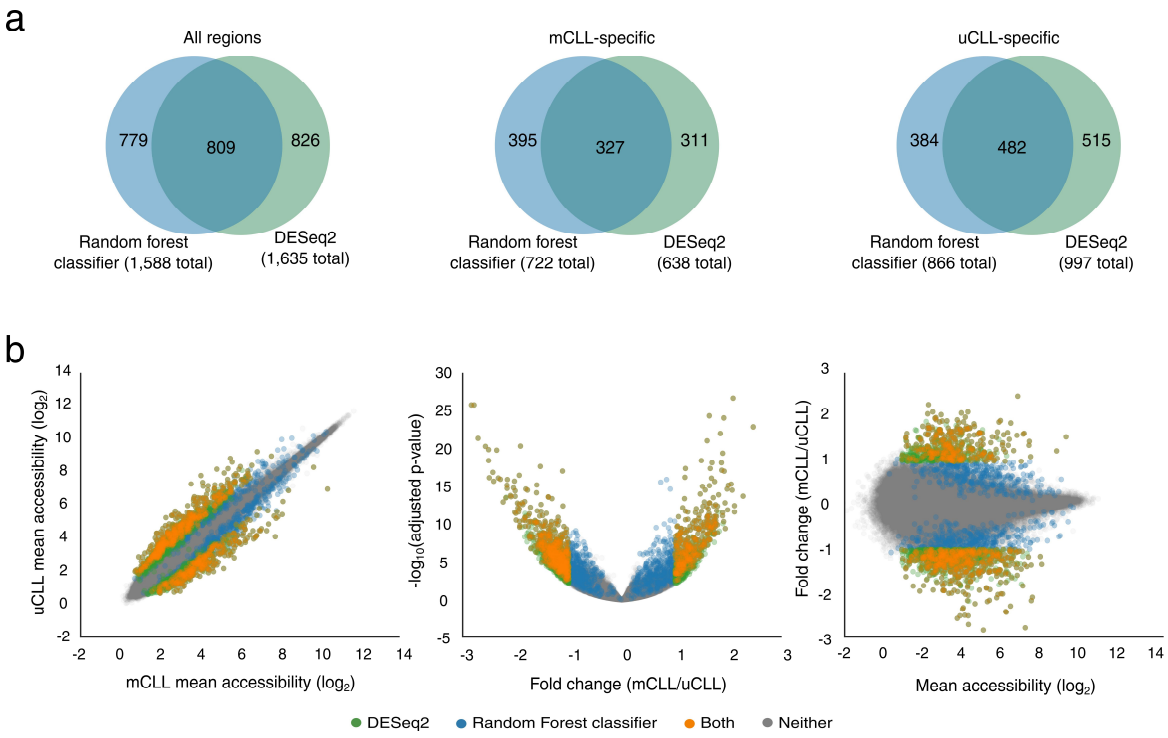

Supplementary Figure 9

Subtype-specific signature regions overlap with differential ATAC-seq peaks.

a) Venn diagrams showing the overlap between CLL subtype-specific regions identified by the machine learning analysis (left) compared to those identified by differential peak analysis between mCLL and uCLL using DESeq2. b) Scatterplot (left), volcano plot (center) and MA plot (right) comparing the two analytical approaches across all chromatin-accessible regions.

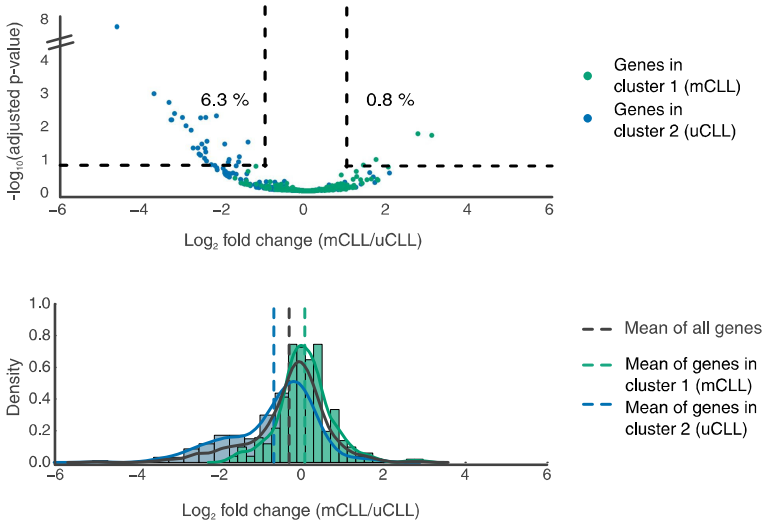

Supplementary Figure 10

Subtype-specific signature regions are weakly associated with differentially expressed genes.

Volcano plot (top) and histogram (bottom) showing gene expression differences between mCLL and uCLL samples for genes that are co-localized with subtype-specific signature regions. Percentage values are based on the number of genes that were significantly differentially expressed in the RNA-seq analysis.

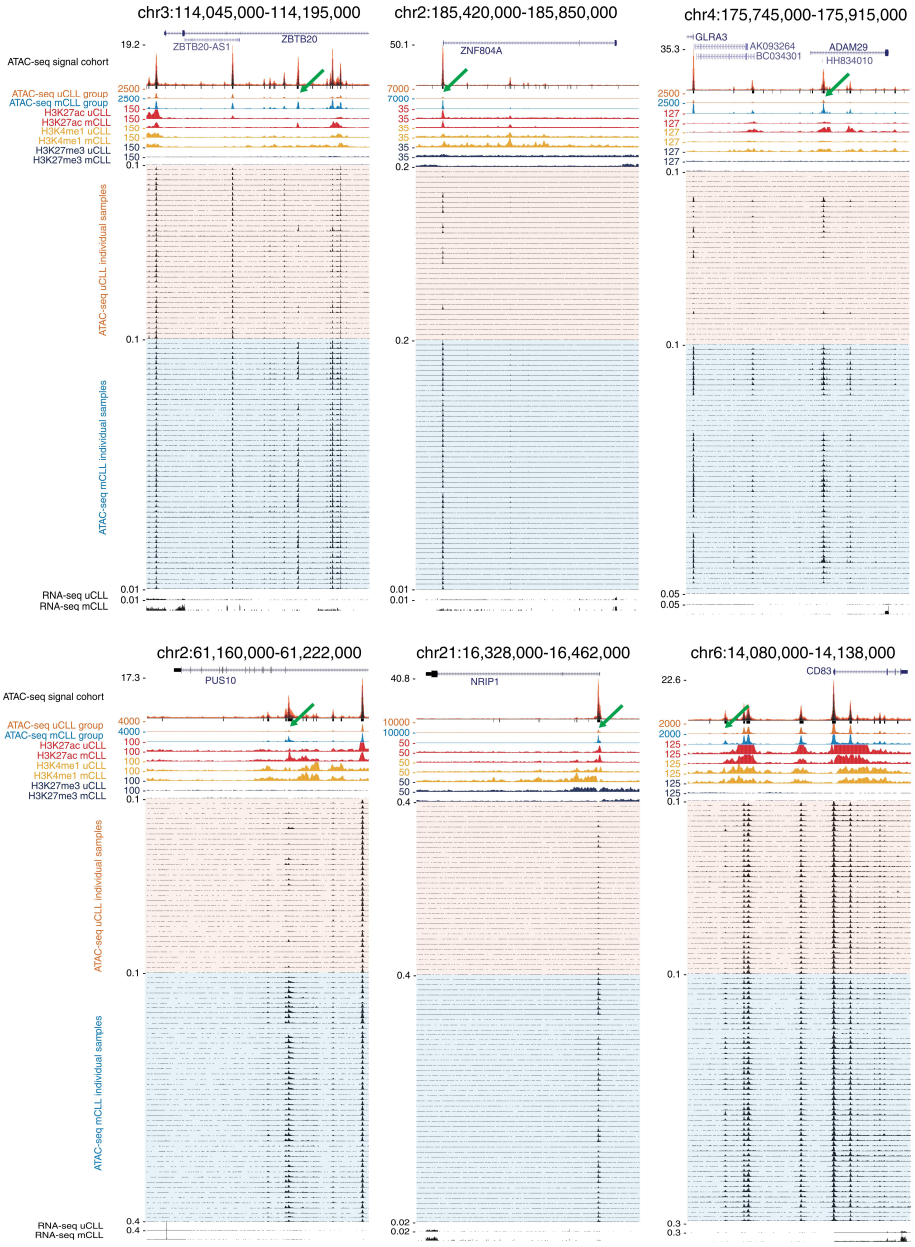

Supplementary Figure 11

Signature regions specific to mCLL show strong differences between disease subtypes but also heterogeneity within each subtype.

Genome browser plots for six gene loci that contain mCLL-specific signature regions (indicated by the green arrows). All ATAC-seq tracks were normalized by read depth to improve comparability between samples.

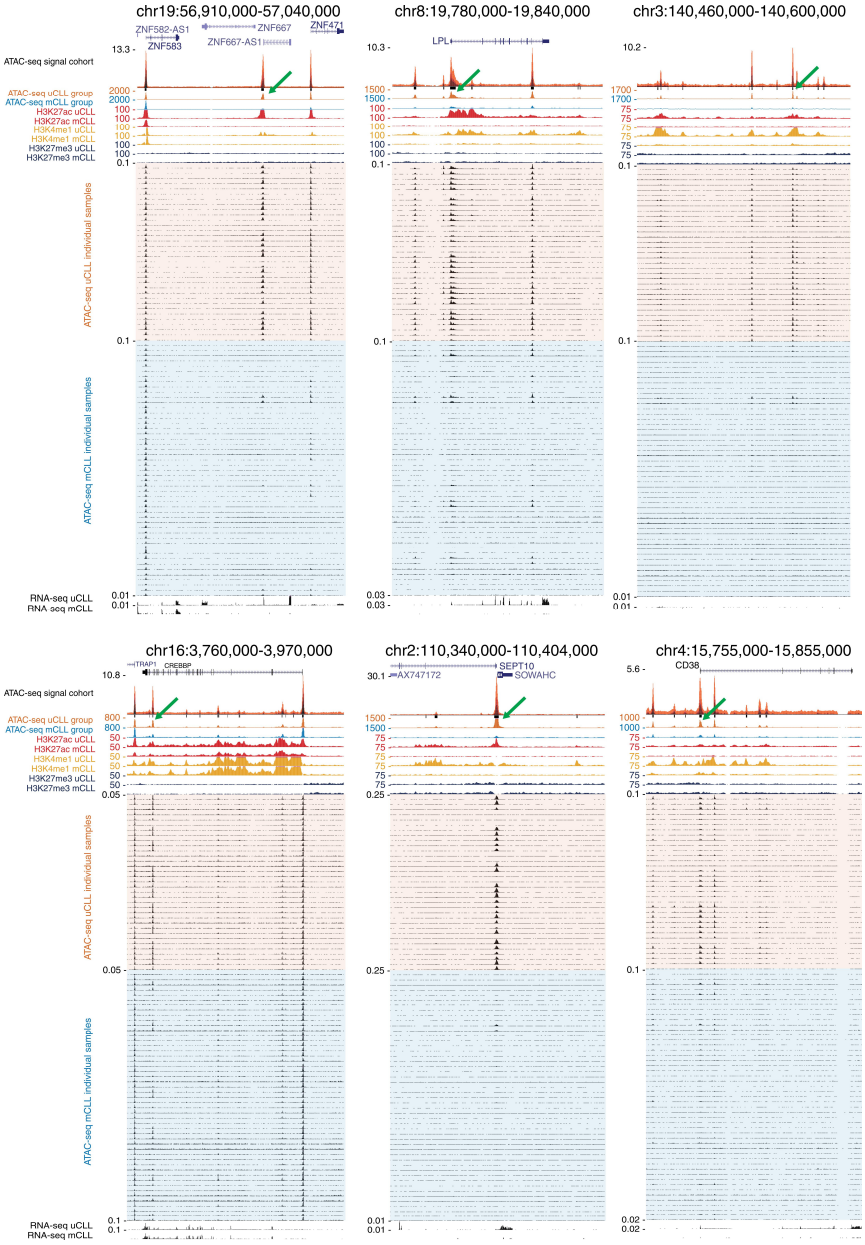

Supplementary Figure 12

Signature regions specific to uCLL show strong differences between disease subtypes but also heterogeneity within each subtype.

Genome browser plots for six gene loci that contain uCLL-specific signature regions (indicated by the green arrows). All ATAC-seq tracks were normalized by read depth to improve comparability between samples.

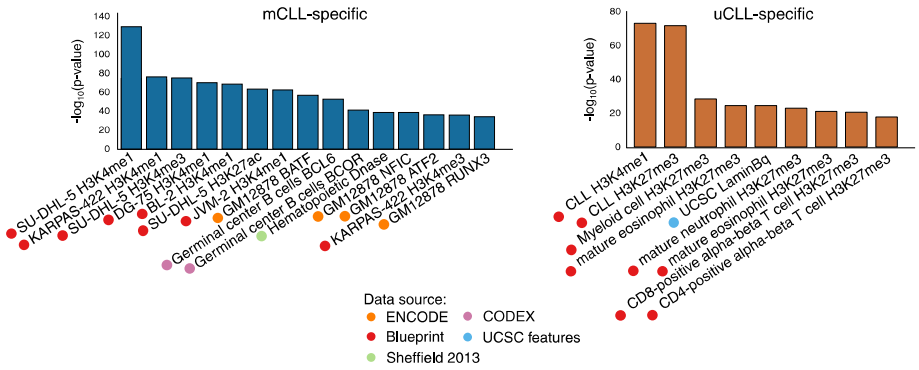

Supplementary Figure 13

Enrichment analysis for differential ATAC-seq peaks yields similar results as for the subtype-specific signature regions.

Complementing and validating the enrichment analysis shown in Figure 3g, this diagram lists the most highly enriched LOLA region sets for mCLL-specific (blue) and uCLL-specific (orange) differential peaks identified using DESeq2.

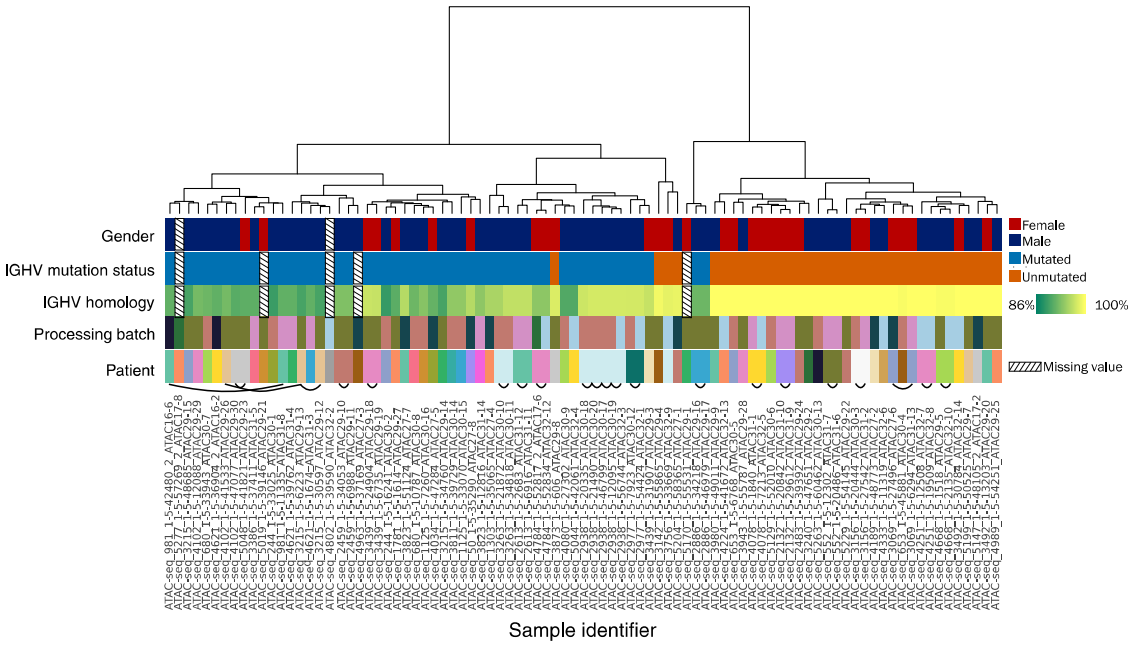

Supplementary Figure 14

Clustering based on CLL subtype-specific signature regions reflects IGHV mutation status.

Hierarchical clustering of all CLL samples based on sample-wise correlation of chromatin accessibility for the most discriminatory regions that were identified between the *IGHV*-mutated and the *IGHV*-unmutated disease subtype. The clustering tree is annotated with clinical data, and samples from the same patient are connected by curved black lines.

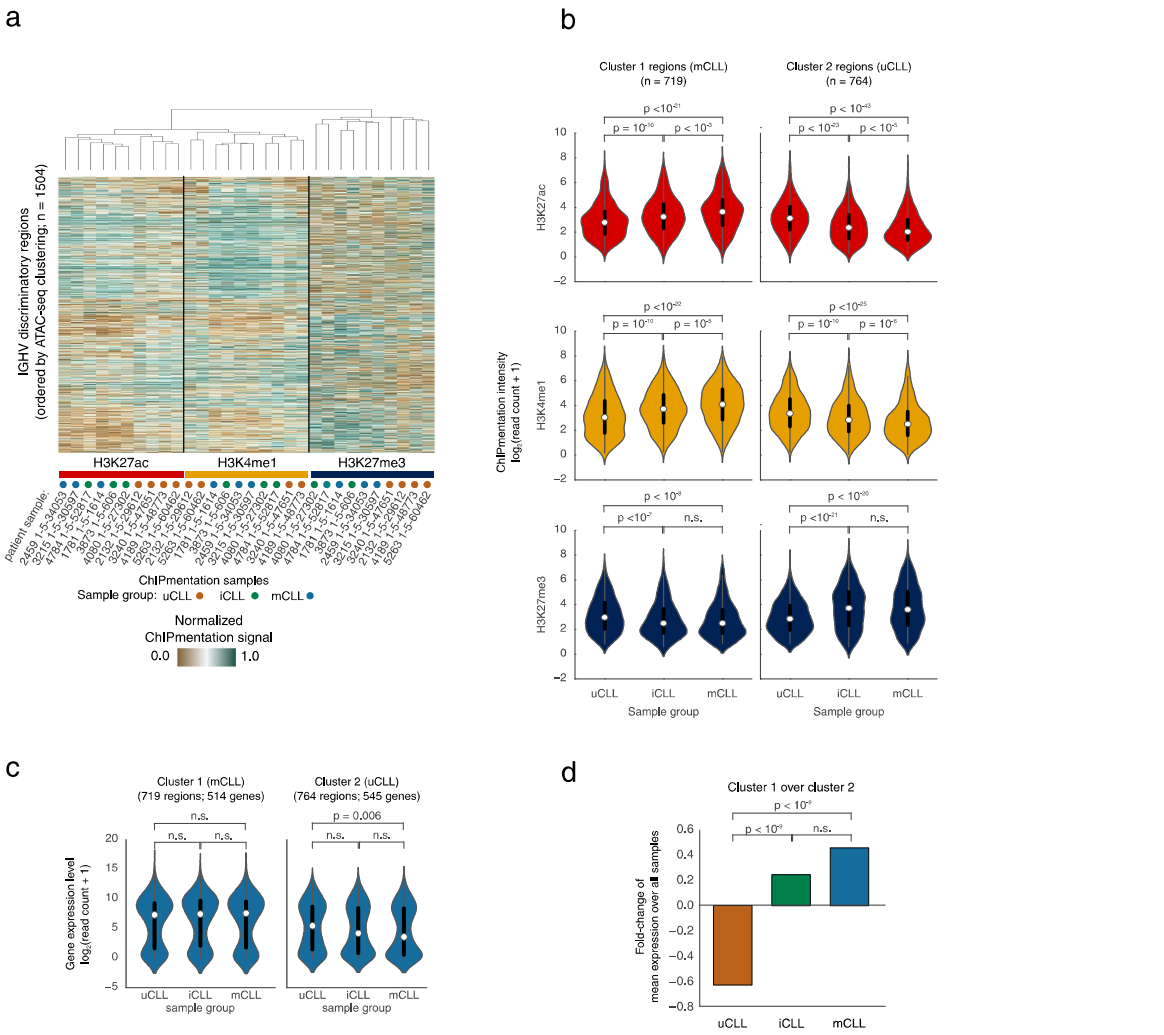

Supplementary Figure 15

Histone marks and gene expression confirm the intermediate character of the iCLL sample cluster.

a) Hierarchical clustering and heatmap visualizing the ChIPmentation signal for three histone marks (H3K4me1, H3K27ac, H3K27me3) in ten CLL samples comprising three disease subtypes (mCLL, iCLL, uCLL). Regulatory regions were selected and sorted in the same way as in Figure 3c. b) Violin plots showing the distribution of ChIPmentation levels for each histone mark in the same regulatory regions as in panel a, grouped by disease subtype. In all panels, significance was assessed using the Mann-Whitney *U* test, and comparisons with *p*-values above 0.05 were labeled as not significant (n.s.). c) Mean gene expression values for genes associated with the regulatory regions from panel a, grouped by disease subtype. d) Barplot showing the mean fold change of genes associated with regulatory elements in cluster 1 (mCLL regions) over genes associated with cluster 2 (uCLL regions) across all genes, grouped by disease subtypes. Significance was assessed using the Mann-Whitney *U* test, and comparisons with *p*-values above 0.05 were labeled as not significant (n.s.).

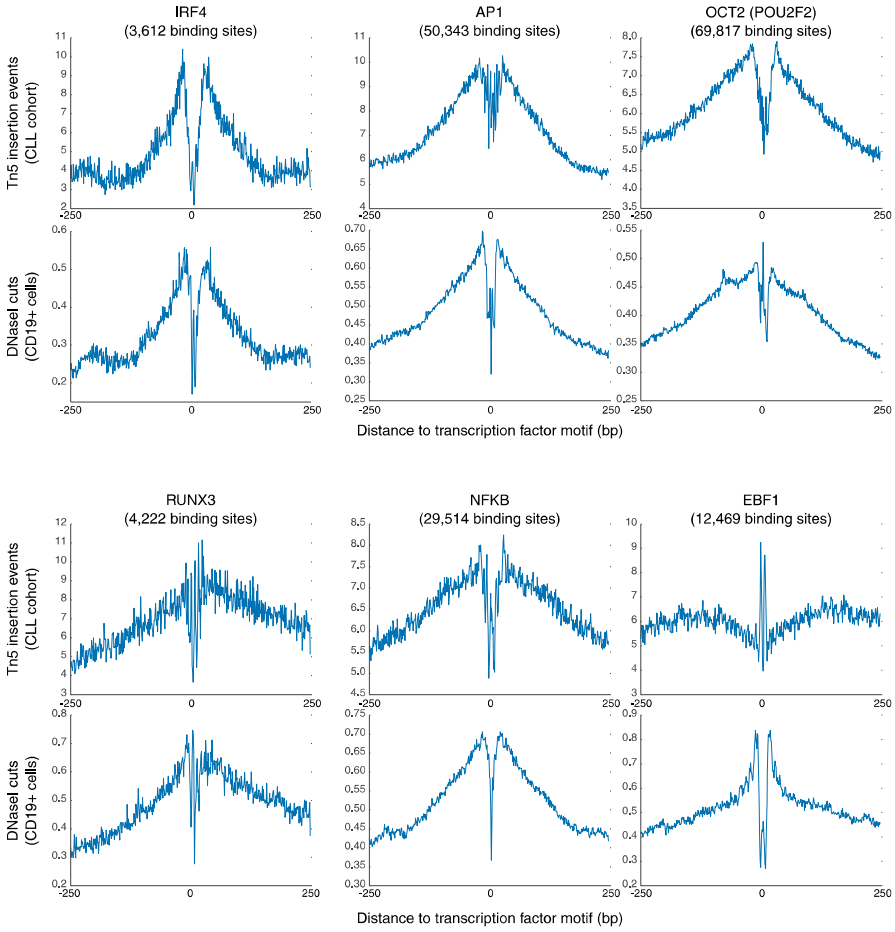

Supplementary Figure 16

Transcription factor footprints for ATAC-seq and DNase-seq are similar.

Footprinting diagrams showing the frequency of Tn5 transposase insertion events (for ATAC-seq) and DNase I cutting sites (for DNase-seq, based on data for CD19+ B cells from the Roadmap Epigenomics project) across a 500 basepair window around DNA binding motifs of transcription factors involved in B cell development.

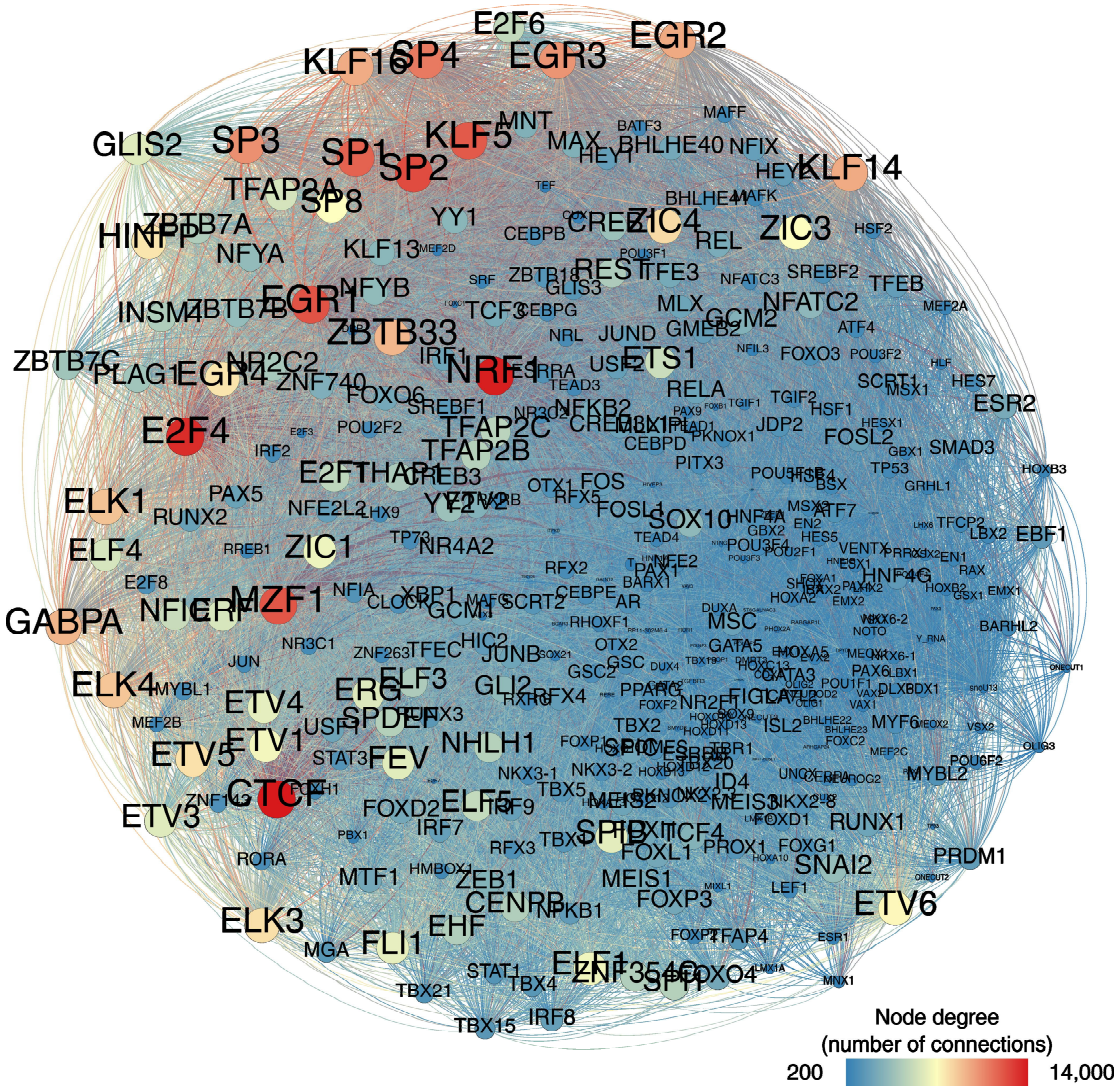

Supplementary Figure 17

Cohort-level gene regulatory network identifies transcription factors relevant to CLL.

Gene regulatory network of CLL inferred from footprint predictions of transcription factor binding, based on the ATAC-seq data of all CLL samples. Only nodes with more than 200 connections are shown.

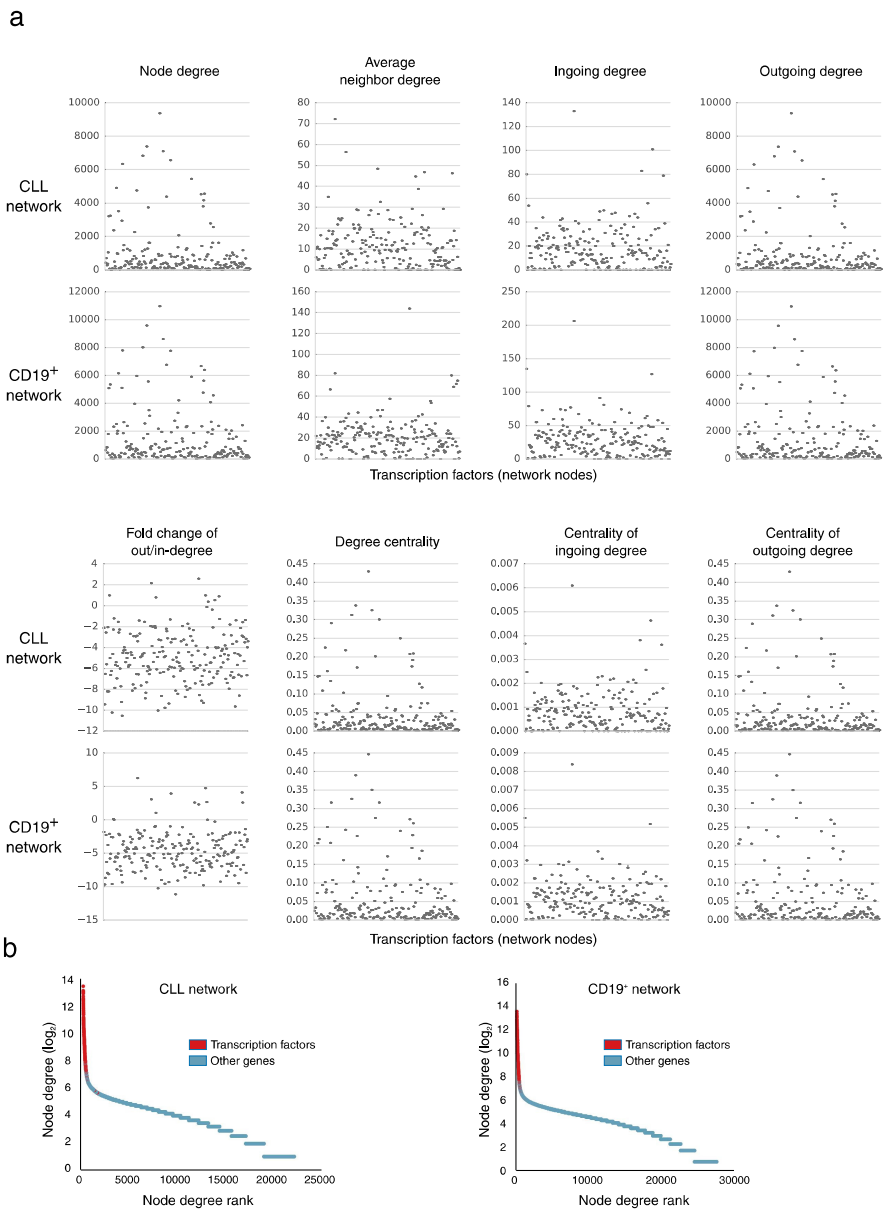

Supplementary Figure 18

Footprinting-based gene regulatory networks for ATAC-seq in CLL and DNase-seq in B cells show similar properties.

a) Structural properties of gene regulatory networks inferred from ATAC-seq data for the CLL cohort and from DNase-seq data for CD19+ B cells. b) Number of connections for all genes in the two gene regulatory networks (transcription factors are shown in red).

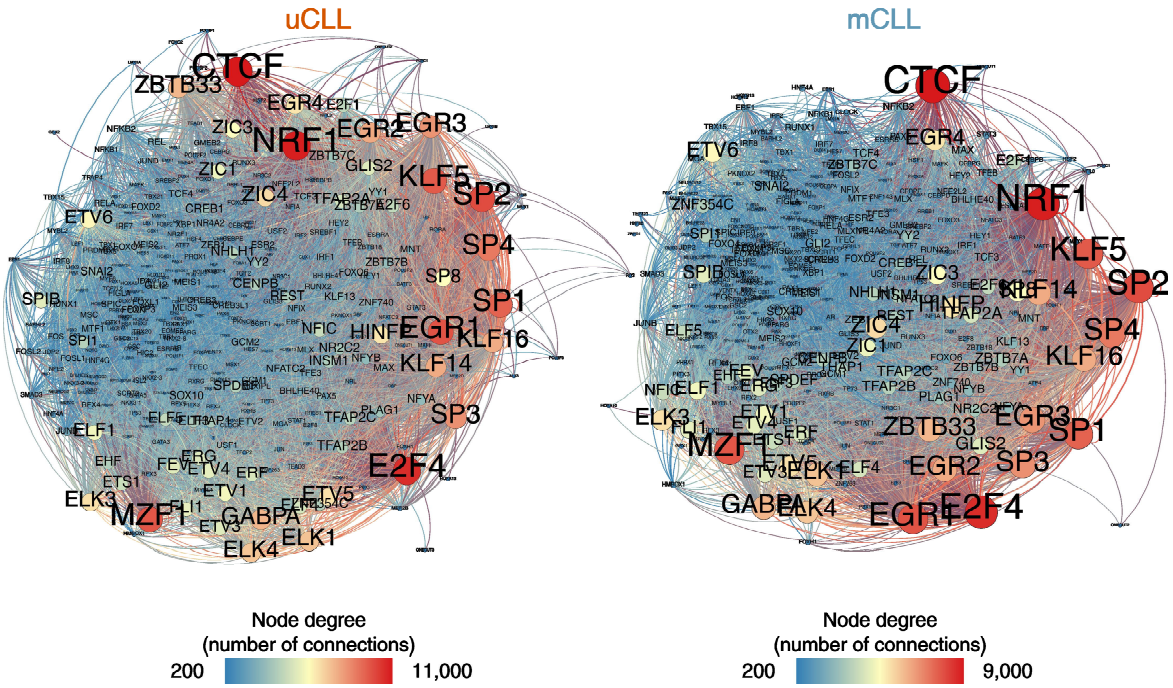

Supplementary Figure 19

Gene regulatory networks for mCLL and uCLL samples are globally similar.

Gene regulatory networks inferred based on the *IGHV*-unmutated samples (uCLL, left) and based on the *IGHV*-mutated samples (mCLL, right). Only nodes with more than 200 connections are shown.

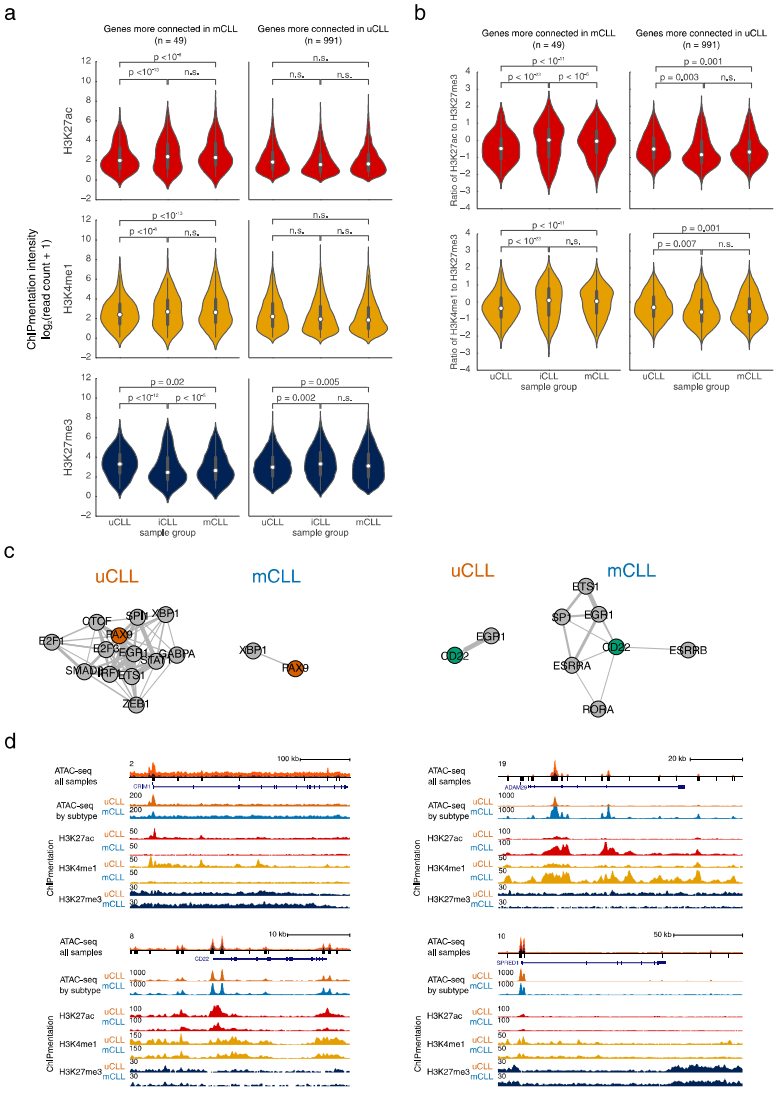

Supplementary Figure 20

Disease subtype-specific networks detect differentially regulated genes and genomic regions.

a) Violin plots showing the distribution of ChIPmentation levels for each histone mark in regulatory regions associated with genes that are differentially connected between the subtype-specific networks. b) Violin plots showing the ratio between the ChIPmentation signal for histone marks associated with active (H3K4me1, H3K27ac) over repressed (H3K27me3) chromatin. c) Subnetworks with the neighbors of PAX9 and CD22, shown separately for the mCLL and uCLL networks. Edge width indicates the strength of the connection as measured by the calculated interaction score. d) ATAC-seq and ChIPmentation signal for three histone marks at representative differentially connected genes between the mCLL and uCLL networks. In panel a and b, significance was assessed using the Mann-Whitney *U* test, and comparisons with *p*-values above 0.05 were labeled as not significant (n.s.).

References

1. Byrd, J. C., Stilgenbauer, S. & Flinn, I. W. Chronic lymphocytic leukemia. *Hematology / the Education Program of the American Society of Hematology. American Society of Hematology. Education Program* 163–183 (2004).

2. Zenz, T., Mertens, D., Küppers, R., Döhner, H. & Stilgenbauer, S. From pathogenesis to treatment of chronic lymphocytic leukaemia. *Nature Reviews Cancer* **10**, 37–50 (2010). URL http://www.nature.com/doifinder/10.1038/nrc2764.

3. Damle, R. N. *et al.* Ig V gene mutation status and CD38 expression as novel prognostic indicators in chronic lymphocytic leukemia. *Blood* **94**, 1840–1847 (1999).

4. Hamblin, T. J., Davis, Z., Gardiner, A., Oscier, D. G. & Stevenson, F. K. Unmutated Ig V(H) genes are associated with a more aggressive form of chronic lymphocytic leukemia. *Blood* **94**, 1848–1854 (1999).

5. Tobin, G. *et al.* Somatically mutated Ig VH3-21 genes characterize a new subset of chronic lymphocytic leukemia. *Blood* **99**, 2262–2264 (2002). URL http://www.bloodjournal.org/cgi/doi/10.1182/blood.V99.6.2262.

6. Agathangelidis, A. *et al.* Stereotyped B-cell receptors in one third of chronic lymphocytic leukemia: towards a molecular classification with implications for targeted therapeutic interventions. *Blood* **119**, 4467–4476 (2012).

7. Rossi, D. *et al.* Stereotyped B-Cell Receptor Is an Independent Risk Factor of Chronic Lymphocytic Leukemia Transformation to Richter Syndrome Stereotyped B-Cell Receptor Is an Independent Risk Factor of **15**, 4415–4422 (2009).

8. Di Giovanni, S., Valentini, G., Carducci, P. & Giallonardo, P. Beta-2-Microglobulin Is a Reliable Tumor Marker in Chronic Lymphocytic Leukemia. *Acta Haematologica* **81**, 181–185 (1989). URL http://www.karger.com/DOI/10.1159/000205558.

9. Hallek, M. *et al.* Elevated serum thymidine kinase levels identify a subgroup at High Risk of Disease Progression in Early, Nonsmoldering Chronic Lymphocytic Leukemia. *Blood* **93**, 1732–7 (1999). URL http://www.ncbi.nlm.nih.gov/pubmed/10029603.

10. Döhner, H. *et al.* Genomic Aberrations and Survival in Chronic Lymphocytic Leukemia. *New England Journal of Medicine* **343**, 1910–1916 (2000). URL http://www.nejm.org/doi/abs/10.1056/NEJM200012283432602.

11. Rossi, D. *et al.* CME Article Integrated mutational and cytogenetic analysis identifies new prognostic subgroups in chronic lymphocytic leukemia **121**, 1403–1412 (2013).

12. Baliakas, P. *et al.* Recurrent mutations refine prognosis in chronic lymphocytic leukemia. *Leukemia* 1–8 (2014). URL http://www.ncbi.nlm.nih.gov/pubmed/24943832.

13. Oscier, D. G. *et al.* The clinical significance of NOTCH1 and SF3B1 mutations in the UK LRF CLL4 trial. *Blood* **121**, 468–75 (2013). URL http://www.ncbi.nlm.nih.gov/pubmed/23086750.

14. Stilgenbauer, S. *et al.* Gene Mutations and Treatment Outcome in Chronic Lymphocytic Leukemia. *Blood* **123**, 3247–3255 (2014).

15. Crespo, M. *et al.* ZAP-70 expression as a surrogate for immunoglobulin-variable-region mutations in chronic lymphocytic leukemia. *The New England Journal of Medicine* **348**, 1764–1775 (2003).

16. Ferreira, P. G. *et al.* Transcriptome characterization by RNA sequencing identifies a major molecular and clinical subdivision in chronic lymphocytic leukemia. *Genome Research* **24**, 212–226 (2014). URL http://genome.cshlp.org/cgi/doi/10.1101/gr.152132.112.

17. Landau, D. A. *et al.* Mutations driving CLL and their evolution in progression and relapse. *Nature* (2015). URL http://www.nature.com/doifinder/10.1038/nature15395.

18. Puente, X. S. *et al.* Non-coding recurrent mutations in chronic lymphocytic leukaemia. *Nature* (2015). URL http://www.nature.com/doifinder/10.1038/nature14666.

19. Lawrence, M. S. *et al.* Mutational heterogeneity in cancer and the search for new cancer-associated genes. *Nature* **499**, 214–8 (2013). URL http://dx.doi.org/10.1038/nature12213.

20. Kulis, M. *et al.* Epigenomic analysis detects widespread gene-body DNA hypomethylation in chronic lymphocytic leukemia. *Nature Genetics* **44**, 1236–1242 (2012). URL http://dx.doi.org/10.1038/ng.2443.

21. Landau, D. *et al.* Locally Disordered Methylation Forms the Basis of Intratumor Methylome Variation in Chronic Lymphocytic Leukemia. *Cancer Cell* **26**, 813–825 (2014). URL http://linkinghub.elsevier.com/retrieve/pii/S1535610814004164.

22. Oakes, C. C. *et al.* Evolution of DNA Methylation Is Linked to Genetic Aberrations in Chronic Lymphocytic Leukemia. *Cancer Discovery* **4**, 348–361 (2014). URL http://cancerdiscovery.aacrjournals.org/cgi/doi/10.1158/2159-8290.CD-13-0349.

23. Queirós, a. C. *et al.* A B-cell epigenetic signature defines three biologic subgroups of chronic lymphocytic leukemia with clinical impact. *Leukemia* **29**, 598–605 (2015). URL http://www.ncbi.nlm.nih.gov/pubmed/25151957http://www.nature.com/doifinder/10.1038/leu.2014.252.

24. Baylin, S. B. & Jones, P. A. A decade of exploring the cancer epigenome — biological and translational implications. *Nat Rev Cancer* **11**, 726–734 (2011). URL http://dx.doi.org/10.1038/nrc3130.

25. Buenrostro, J. D., Giresi, P. G., Zaba, L. C., Chang, H. Y. & Greenleaf, W. J. Transposition of native chromatin for fast and sensitive epigenomic profiling of open chromatin, DNA-binding proteins and nucleosome position. *Nature methods* **10**, 1213–8 (2013). URL http://www.pubmedcentral.nih.gov/articlerender.fcgi?artid=3959825{&}tool=pmcentrez{&}rendertype=abstract.

26. Schmidl, C., Rendeiro, A. F., Sheffield, N. C. & Bock, C. ChIPmentation: fast, robust, low-input ChIP-seq for histones and transcription factors. *Nature Methods* (2015). URL http://www.nature.com/doifinder/10.1038/nmeth.3542.

27. Risca, V. I. & Greenleaf, W. J. Unraveling the 3D genome: genomics tools for multiscale exploration. *Trends in Genetics* **31**, 357–372 (2015). URL http://linkinghub.elsevier.com/retrieve/pii/S0168952515000633.

28. Kundaje, A. *et al.* Integrative analysis of 111 reference human epigenomes. *Nature* **518**, 317–330 (2015). URL http://www.nature.com/doifinder/10.1038/nature14248.

29. Stevenson, F. K. F., Krysov, S., Davies, A. J., Steele, A. J. & Packham, G. B-cell receptor signaling in chronic lymphocytic leukemia. *Blood* **118**, 4313–4320 (2011). URL http://bloodjournal.hematologylibrary.org/content/118/16/4313.short$\delimiter"026E30F$nhttp://www.ncbi.nlm.nih.gov/pubmed/21816833.

30. Ecker, S., Pancaldi, V., Rico, D. & Valencia, A. Higher gene expression variability in the more aggressive subtype of chronic lymphocytic leukemia. *Genome medicine* **7**, 8 (2015). URL http://www.pubmedcentral.nih.gov/articlerender.fcgi?artid=4308895{&}tool=pmcentrez{&}rendertype=abstract.

31. Sheffield, N. C. & Bock, C. LOLA : Enrichment analysis for genomic region sets and regulatory elements in R and Bioconductor 1–3 (2015).

32. Morabito, F. *et al.* Surrogate molecular markers for IGHV mutational status in chronic lymphocytic leukemia for predicting time to first treatment. *Leukemia Research* **39**, 840–845 (2016). URL http://dx.doi.org/10.1016/j.leukres.2015.05.005.

33. Nikitin, E. a. *et al.* Expression level of lipoprotein lipase and dystrophin genes predict survival in B-cell chronic lymphocytic leukemia. *Leukemia & lymphoma* **48**, 912–922 (2007).

34. Oppezzo, P. *et al.* The LPL/ADAM29 expression ratio is a novel prognosis indicator in chronic lymphocytic leukemia. *Blood* **106**, 650–657 (2005). URL http://www.bloodjournal.org/cgi/doi/10.1182/blood-2004-08-3344.

35. Hock, B. *et al.* Release and clinical significance of soluble CD83 in chronic lymphocytic leukemia. *Leukemia Research* **33**, 1089–1095 (2009). URL http://dx.doi.org/10.1016/j.leukres.2009.01.001http://linkinghub.elsevier.com/retrieve/pii/S014521260900006X.

36. Malavasi, F. *et al.* CD38 and chronic lymphocytic leukemia: a decade later. *Blood* **118**, 3470–3478 (2011). URL http://www.bloodjournal.org/cgi/doi/10.1182/blood-2011-06-275610.

37. Forconi, F. *et al.* The normal IGHV1-69-derived B-cell repertoire contains stereotypic patterns characteristic of unmutated CLL. *Blood* **115**, 71–77 (2010). URL http://www.bloodjournal.org/cgi/doi/10.1182/blood-2009-06-225813.

38. Mathelier, A. *et al.* JASPAR 2014: an extensively expanded and updated open-access database of transcription factor binding profiles. *Nucleic Acids Research* **42**, D142–D147 (2014). URL http://nar.oxfordjournals.org/lookup/doi/10.1093/nar/gkt997.

39. Alizadeh, A. A. *et al.* Toward understanding and exploiting tumor heterogeneity. *Nature Medicine* **21**, 1–8 (2015). URL http://dx.doi.org/10.1038/nm.3915.

40. Sung, M.-H., Baek, S. & Hager, G. L. Genome-wide footprinting: ready for prime time? *Nat Meth* **13**, 222–228 (2016). URL http://dx.doi.org/10.1038/nmeth.3766http://10.1038/nmeth.3766.

41. Rosati, E. *et al.* Constitutively activated Notch signaling is involved in survival and apoptosis resistance of B-CLL cells. *Blood* **113**, 856–865 (2009).

42. Tomic, J. *et al.* Aberrant interferon-signaling is associated with aggressive chronic lymphocytic leukemia Aberrant interferon-signaling is associated with aggressive chronic lymphocytic leukemia **117**, 2668–2680 (2013).

43. Mittal, A. K. *et al.* Role of CTLA4 in the Proliferation and Survival of Chronic Lymphocytic Leukemia. *PLoS ONE* **8**, e70352 (2013). URL http://dx.plos.org/10.1371/journal.pone.0070352.

44. Klein, U. *et al.* Gene expression profiling of B cell chronic lymphocytic leukemia reveals a homogeneous phenotype related to memory B cells. *The Journal of experimental medicine* **194**, 1625–1638 (2001).

45. Rosenwald, A. *et al.* Relation of gene expression phenotype to immunoglobulin mutation genotype in B cell chronic lymphocytic leukemia. *The Journal of experimental medicine* **194**, 1639–47 (2001). URL http://www.pubmedcentral.nih.gov/articlerender.fcgi?artid=2193523{&}tool=pmcentrez{&}rendertype=abstract.

46. Basso, K. *et al.* Reverse engineering of regulatory networks in human B cells. *Nature genetics* **37**, 382–390 (2005).

47. Lefebvre, C. *et al.* A human B-cell interactome identifies MYB and FOXM1 as master regulators of proliferation in germinal centers. *Molecular systems biology* **6**, 377 (2010). URL http://dx.doi.org/10.1038/msb.2010.31.

48. Yepes, S., Torres, M. M. & López-Kleine, L. Regulatory network reconstruction reveals genes with prognostic value for chronic lymphocytic leukemia. *BMC Genomics* **16**, 1002 (2015). URL http://www.biomedcentral.com/1471-2164/16/1002.

49. Bock, C. *et al.* Reference Maps of human ES and iPS cell variation enable high-throughput characterization of pluripotent cell lines. *Cell* **144**, 439–52 (2011). URL http://www.pubmedcentral.nih.gov/articlerender.fcgi?artid=3063454{&}tool=pmcentrez{&}rendertype=abstract.

50. Buenrostro, J. D. *et al.* Single-cell chromatin accessibility reveals principles of regulatory variation. *Nature* (2015). URL http://www.nature.com/doifinder/10.1038/nature14590.

51. Jin, W. *et al.* Genome-wide detection of DNase I hypersensitive sites in single cells and FFPE tissue samples. *Nature* (2015). URL http://www.nature.com/doifinder/10.1038/nature15740.

52. Jiang, H., Lei, R., Ding, S.-W. & Zhu, S. Skewer: a fast and accurate adapter trimmer for next-generation sequencing paired-end reads. *BMC bioinformatics* **15**, 182 (2014). URL http://www.biomedcentral.com/1471-2105/15/182.

53. Langmead, B. & Salzberg, S. L. Fast gapped-read alignment with Bowtie 2. *Nature Methods* **9**, 357–359 (2012). {#}14603.

54. Tarasov, A., Vilella, A. J., Cuppen, E., Nijman, I. J. & Prins, P. Sambamba: Fast processing of NGS alignment formats. *Bioinformatics* **31**, 2032–2034 (2015).

55. Quinlan, A. R. & Hall, I. M. BEDTools: a flexible suite of utilities for comparing genomic features. *Bioinformatics (Oxford, England)* **26**, 841–2 (2010). URL http://www.pubmedcentral.nih.gov/articlerender.fcgi?artid=2832824{&}tool=pmcentrez{&}rendertype=abstract.

56. Zhang, Y. *et al.* Model-based analysis of ChIP-Seq (MACS). *Genome biology* **9**, R137 (2008). URL http://www.pubmedcentral.nih.gov/articlerender.fcgi?artid=2592715{&}tool=pmcentrez{&}rendertype=abstract.

57. Hoffman, M. M. *et al.* Integrative annotation of chromatin elements from ENCODE data. *Nucleic acids research* **41**, 827–41 (2013). URL http://www.pubmedcentral.nih.gov/articlerender.fcgi?artid=3553955{&}tool=pmcentrez{&}rendertype=abstract.

58. Bolger, A. M., Lohse, M. & Usadel, B. Trimmomatic: A flexible trimmer for Illumina sequence data. *Bioinformatics* **30**, 2114–2120 (2014).

59. Langmead, B., Trapnell, C., Pop, M. & Salzberg, S. L. Ultrafast and memory-efficient alignment of short DNA sequences to the human genome. *Genome biology* **10**, R25 (2009). URL http://www.ncbi.nlm.nih.gov/entrez/query.fcgi?cmd=Retrieve{&}db=PubMed{&}dopt=Citation{&}list{_}uids=19261174.

60. Hensman, J., Papastamoulis, P., Glaus, P., Honkela, A. & Rattray, M. Fast and accurate approximate inference of transcript expression from RNA-seq data. *Bioinformatics* **31**, 3881–3889 (2015). 1412.5995.

61. Love, M. I., Anders, S. & Huber, W. *Differential analysis of count data - the DESeq2 package* (2014). URL http://biorxiv.org/lookup/doi/10.1101/002832.

62. Ernst, J. & Kellis, M. Large-scale imputation of epigenomic datasets for systematic annotation of diverse human tissues. *Nature Biotechnology* (2015). URL http://www.nature.com/doifinder/10.1038/nbt.3157.

63. Rosenbloom, K. R. *et al.* The UCSC Genome Browser database: 2015 update. *Nucleic Acids Research* **43**, D670–D681 (2015). URL http://nar.oxfordjournals.org/lookup/doi/10.1093/nar/gku1177.

64. Pedregosa, F. & Varoquaux, G. Scikit-learn: Machine Learning in Python. *Journal of Machine ...* **12**, 2825–2830 (2011). URL http://jmlr.csail.mit.edu/papers/volume12/pedregosa11a/pedregosa11a.pdf. 1201.0490.

65. Sheffield, N. C. *et al.* predict tissue identity , transcription factor binding , and long-range interactions Patterns of regulatory activity across diverse human cell types predict tissue identity , transcription factor binding , and long-range interactions 777–788 (2013).

66. Liu, T. *et al.* Cistrome: an integrative platform for transcriptional regulation studies. *Genome biology* **12**, R83 (2011). URL http://genomebiology.com/2011/12/8/R83.

67. Adams, D. *et al.* BLUEPRINT to decode the epigenetic signature written in blood. *Nature Biotechnology* **30**, 224–226 (2012). URL http://dx.doi.org/10.1038/nbt.2153$\delimiter"026E30F$npapers2://publication/doi/10.1038/nbt.2153.

68. Bailey, T. L. *et al.* MEME Suite: Tools for motif discovery and searching. *Nucleic Acids Research* **37**, 202–208 (2009).

69. Wang, B., Cunningham, J. M. & (Holly) Yang, X. Seq2pathway: an R/Bioconductor package for pathway analysis of next-generation sequencing data: Fig. 1. *Bioinformatics* **31**, 3043–3045 (2015). URL http://bioinformatics.oxfordjournals.org/lookup/doi/10.1093/bioinformatics/btv289.

70. Sherwood, R. I. *et al.* Discovery of directional and nondirectional pioneer transcription factors by modeling DNase profile magnitude and shape. *Nature biotechnology* **32**, 171–8 (2014). URL http://www.pubmedcentral.nih.gov/articlerender.fcgi?artid=3951735{&}tool=pmcentrez{&}rendertype=abstract.

71. Qu, K. *et al.* Individuality and Variation of Personal Regulomes in Primary Human T Cells. *Cell Systems* **1**, 51–61 (2015). URL http://linkinghub.elsevier.com/retrieve/pii/S2405471215000095.

72. Hagberg, A. A., Schult, D. A. & Swart, P. J. Exploring network structure, dynamics, and function using {NetworkX}. In *Proceedings of the 7th Python in Science Conference (SciPy2008)*, 11–15 (Pasadena, CA USA, 2008).